INTERACTION OF AN UPPER-TROPOSPHERIC JET WITH A SQUALL LINE ORIGINATING ALONG A COLD FRONTAL BOUNDARY

BY

DANIEL M. STECHMAN

THESIS

Submitted in partial fulfillment of the requirements
for the degree of Master of Science in Atmospheric Sciences
in the Graduate College of the
University of Illinois at Urbana-Champaign, 2015

Urbana, Illinois

Advisers:

Professor Robert M. Rauber
Professor Greg M. McFarquhar
Dr. Brian F. Jewett

Abstract

On 8 June 2003, an expansive squall line along a surface cold frontal boundary was sampled during the Bow Echo and Mesoscale Convective Vortex Experiment. The Naval Research Laboratory P-3 aircraft and the National Oceanic and Atmospheric Administration P-3 aircraft simultaneously sampled the leading and trailing edge of this squall line, respectively, with X-band Doppler radars. Data from these two airborne radar systems have been synthesized to produce a quad-Doppler analysis of the squall line, yielding a detailed three-dimensional kinematic analysis of its structure. A simulation of the squall line was carried out using the Weather Research and Forecasting model to complement the quad-Doppler analysis. The simulation employed a 3 km, convection-allowing, nested domain centered over the quad-Doppler domain, along with a 9 km parent domain to capture the larger synoptic-scale cyclone.

The quad-Doppler analysis reveals that the convective line was embedded within the upper-tropospheric jetstream, causing local decelerations and deviations in the jet-level flow. The vertical transport of low momentum air from the boundary layer via convective updrafts is shown to significantly decelerate jet-level flow. The convective updrafts are also found to tilt baroclinically generated horizontal shear into the vertical, contributing to the generation of counter-rotating ribbons of vertical vorticity parallel to the squall line. The orientation of these ribbons parallel to the squall line was found to couple with vertical momentum transport to produce the observed decelerations within the jetstream. Obstacle-flow is considered as a possible factor in the observed flow pattern, though an analysis of pressure perturbations in the horizontal are used to show this is not an appropriate theory for this system.

Acknowledgments

Table of Contents

1. Introduction

Summertime mid-latitude extratropical cyclones over the continental United States east of the Rocky Mountains are frequently observed to produce frontal squall lines (Wyss and Emanuel 1988; Bluestein and Jain 1985). Lifting associated with the cold front and the incipient squall line convective dynamics help to initiate and sustain these systems (e.g., Ross and Orlanski 1978; Houze 2004). Newton (1950) initially suggested that a cold pool was key in the propagation of squall lines, a theory which has been further explained by others, such as Rotunno et al. (1988). However, Stoelinga et al. (2003) argued that cold pools were not in fact necessary for the maintenance and propagation of squall lines, and that cold fronts aloft are also capable of filling this role.

Convective motions within squall lines are by nature capable of modifying their environment through the vertical advection of various atmospheric quantities. Of particular interest in the present study is the vertical transport of momentum. Convective momentum transport (CMT) is capable of modifying the propagation and evolution of a parent convective system, and the generation or enhancement of severe winds in the boundary layer (Houze et al. 2000; Mechem et al. 2006; Mahoney et al. 2009). A number of studies have calculated and examined momentum budgets for convective systems (Sanders and Emanuel 1977; Houze 1973; LeMone 1983; Gao et al. 1990; Lipps and Hemler 1991; Gallus and Johnson 1992; LeMone and Moncrieff 1994; Yang and Houze 1996; Trier et al. 1998), most giving preferential focus to the impacts of downward CMT on storm structure and near-surface flow. It is hypothesized in the present study that upward CMT of low momentum air into the upper-troposphere within a squall line is capable of locally disrupting the environmental flow associated with the jetstream, a phenomenon that to our knowledge, has not been previously explored in the literature.

In addition to transporting momentum, convective updrafts are capable of tilting and stretching baroclinically-induced horizontal shear vorticity into the vertical, producing counter-rotating couplets of vertical vorticity about the updraft axis. This phenomenon has been primarily discussed in the context of supercells (e.g., Schlesinger 1975; Kropfli and Miller 1976; Wilhelmson and Klemp 1978). Wakimoto et al. (2015) noted that there are surprisingly few observational studies analyzing the system-wide vertical vorticity generation and structure within mesoscale convective systems (MCSs). Biggerstaff and Houze (1991a,b) and Zhang et al. (1989) showed that bands of cyclonic and anticyclonic vertical vorticity were present in the 10-11 June 1985 Preliminary Regional Experiment for Stormscale Operational Research Meteorology (PRE-STORM) squall line, parallel to the convective line. Wakimoto et al. (2015) analyzed the 2 June 2003 Bow Echo and Mesoscale Convective Vortex Experiment (BAMEX; Davis et al. 2004) squall line, which moved along a warm front. Their study focused on bands of cyclonic and anticyclonic vertical vorticity in the low levels formed through tilting and stretching of horizontal vorticity, with couplets of enhanced vertical vorticity contributing to the formation of embedded bow echoes. To our knowledge, there are currently no documented analyses of jetstream-level vertical vorticity banding parallel to a squall line present along a cold front.

One theory suggests that convective updrafts act as obstacles to the wind field at any given level, in the form of solid cylinders, effectively creating a region of slower winds downshear of, and counter-rotating vertical vorticity pairs aligned with, the updraft (Newton and Newton 1959; Fujita and Grandoso 1968; Fankhauser 1971; Wilhelmson 1974; Kropfli and Miller 1976). This theory has since largely been disproven, most notably by Rotunno and Klemp (1982), who suggested that not only are updrafts more like porous cylinders, with flow into and out of the storm at most levels, but also that the pressure gradient induced across the updraft is aligned with the

environmental shear vector, as opposed to the storm relative wind vector as the obstacle-flow model suggests. Eagleman and Lin (1977) suggested that the presence of a counter-rotating vorticity couplet intrinsically acts to decelerate environmental flow between the couplet, as well as to divert flow to either side of the pair. A recent study by Wang et al. (2010) explored ship wave signatures observed in the vicinity of overshooting convective cloud tops, and notes that diverging mode ship waves are highly suggestive of complex interactions *mimicking* flow around an obstacle.

To further examine these phenomena, the interaction between a frontal squall line and an upper-tropospheric jet was investigated using data collected in an extratropical cyclone on 8 June 2003 during BAMEX. This cyclone tracked through the central and eastern United States, with an extensive cold front at the surface. A squall line developed along and ahead of the surface cold front. High-resolution reflectivity and Doppler velocities from this squall line were collected by two airborne Doppler radars during BAMEX. Many of the storm systems observed during BAMEX were not frontally forced, and as it happens, this is the only BAMEX case yet to be discussed in the literature.

The remainder of this paper describes how these observations and associated model simulation were used to assess interactions between the squall line and upper-tropospheric flow, and is organized as follows. Chapter 2 describes this dataset and the quad-Doppler synthesis employed in this study, along with the setup used for the Weather Research and Forecasting (WRF; Skamarock et al. 2008) model. An overview of the synoptic-scale cyclone along with a synopsis of the associated squall line, is discussed in Chapter 3. Results of the quad-Doppler analysis are presented in Chapter 4, with model simulation results given in Chapter 5. A discussion of these results is provided in Chapter 6, with a summary of the most important findings in Chapter 7.

2. Data Sources and Methods

a. Overview

The BAMEX field campaign studied numerous mesoscale convective systems (MCSs), most producing a bow echo convective structure and/or mesoscale convective vortices (MCVs) (Davis et al. 2004). A large majority of the published work from BAMEX has focused on MCVs (Atkins et al. 2005; Wheatley et al. 2006; Wakimoto et al. 2006a; Hawblitzel et al. 2007; Meng and Zhang 2007; Conzemius et al. 2007; Davis and Trier 2007; Trier and Davis 2007; Jirak and Cotton 2007; Meng and Zhang 2008; Correia and Arritt 2008; Wheatley and Trapp 2008; Galarneau et al. 2009; Davis and Galarneau 2009; Atkins and St. Laurent 2009a,b; James and Johnson 2010; Conzemius and Montgomery 2010). Two aircraft were deployed during BAMEX, each equipped with an airborne Doppler radar, allowing for simultaneous observations of convective systems. Numerous studies have used data collected with these airborne Doppler radars during BAMEX to analyze MCVs, MCSs, and bow echoes through dual- and quad-Doppler radar analyses (Davis et al. 2004; Wakimoto et al. 2004; Cai 2005; Wakimoto et al. 2006b,a; Storm et al. 2007; Smith et al. 2009; Grim et al. 2009; Wakimoto et al. 2015). While airborne Doppler radar data allows for high-quality three-dimensional analyses of a given system, the domain of the single coordinated observation period for this squall line is relatively small at 160 km (east-west) and 200 km (north-south) (Fig. 1), and the ability to track temporal evolution was limited by the absence of subsequent observational passes in the same region. A simulation conducted with the WRF model (version 3.5.1) was used to complement and enhance these observational analyses by extending to larger domains and a longer time period of evolution, while also allowing more process studies.

b. Radar Data

The analysis methods herein closely follow those used by Grim et al. (2009). Observations on 8 June 2003 were made by two P-3 aircraft equipped with 3.2 cm X-band Doppler radars each flown parallel to the convective line. These radars used the fore-aft scanning technique (FAST), the National Oceanic and Atmospheric Administration (NOAA) Tail Doppler Radar (TDR) with a single radar rapidly switching between fore and aft (Jorgensen et al. 1996), and the Electra Doppler Radar (ELDORA) using a separate antenna for both fore and aft measurements. The ELDORA scanning configuration enhanced the along-track resolution to 300 m for that radar (Hildebrand et al. 1996), compared to 1200 m for the NOAA TDR. Use of the FAST method allows for pseudo dual-Doppler wind retrievals for a single aircraft, and pseudo quad-Doppler retrievals when two aircraft sample the same region. Scanning parameters for the NOAA TDR and ELDORA radars are given in Table 1.

The NOAA P-3 flew approximately 10 km to the rear (west) of the line at 4.4 km above mean sea-level (MSL), while the Naval Research Laboratory (NRL) P-3 flew approximately 10 km ahead (east) of the line at 2.2 km MSL. The NOAA P-3 operated on site from 1542 (all times are UTC) to 1853 (Fig. 2). During this time, the NOAA TDR collected data along a single quad-Doppler leg between 1729 and 1747. ELDORA, aboard the NRL P-3, completed the quad-Doppler leg on the other side of the line between 1733 and 1800. The NOAA P-3 experienced engine trouble at 1815, and returned to base before additional quad-Doppler legs could be attained. The ELDORA radar continued to sample the east side of the system, but much further to the south, after the NOAA P-3 departed. ELDORA completed 11 more dual-Doppler legs before returning to base at 2250, though the squall line did not penetrate into the upper-tropospheric jetstream this far south during these observational passes. Analyses of these dual-Doppler legs are not used

5

because winds were not accurately recoverable at jetstream level to the rear of the line due to attenuation and the maximum range of the radar. Furthermore, the low altitude of ELDORA led to beams that were nearly vertical at jetstream level, the region of most interest, significantly reducing the accuracy of horizontal wind recovery at those elevations. The differences in wind recovery between a dual-Doppler and quad-Doppler analysis were examined by completing a dual-Doppler analysis using only the ELDORA dataset and comparing that to the quad-Doppler analysis for the same domain (Fig. 3). As expected, discrepancies in retrieved horizontal velocities were largely constrained to the back end of the line, with the dual-Doppler analysis overestimating velocity by as much as 7 m s^{-1}, particularly in the *v*-component (Fig. 3h) at (39º25', -84º20'; all coordinates given as latitude, longitude), and at (39º50', -84º10'). Attenuation prevented wind recovery in the region centered at (39º35', -84º08') in the dual-Doppler analysis, as seen by the 'V'-shaped notch of missing data (Fig. 3a,b), and a reduction in reflectivity by nearly 25 dBZ (Fig. 3c) when compared to the quad-Doppler analysis in that same location (Fig. 3f). Retrievable velocities surrounding this location were underestimated by as much as 7 m s^{-1} with dual-Doppler alone. This comparison supports the need for quad-Doppler analyses when considering features at high altitudes relative to aircraft positions.

The National Center for Atmospheric Research (NCAR) Solo software (Oye et al. 1995) was used with quality control algorithms outlined in Bell et al. (2013), along with manual hand-edits, to remove aircraft motion and non-meteorological returns from the radar data. Data were then smoothed using a 2-step Leise filter (Leise 1982) to filter wavelengths less than 4 times the horizontal grid spacing, then interpolated to a Cartesian grid, from which horizontal and vertical wind velocities were determined following Jorgensen et al. (1996). This method uses a calculation of vertical velocity at cloud-top to provide the upper boundary condition for a variational

integration of the mass continuity equation, improving the derived vertical velocities in the quad-Doppler region. Jorgensen et al. (1996) showed that for the NOAA TDR and ELDORA radars, at approximately the same altitude above the ground and distance from each other as in the present study, the error in the calculated vertical velocity at cloud-top is ~1.5 times the error in the original observed radial velocity (Fig. 4). A 1 km horizontal and 0.5 km vertical grid resolution were used in the resulting quad-Doppler analysis, contained within the domain outlined in Fig. 1. This analysis includes radar reflectivity and the three-dimensional wind field, from which derived kinematic fields were obtained.

Storm motion was obtained using WSR-88D reflectivity composites of the system and analyzed for both an hour prior to, and following, the quad-Doppler period. Storm motion was found to be from 239° at 13 m s^{-1}, from which all storm-relative flow determinations for this dataset were calculated.

c. WRF Simulation

The WRF model simulation of the 8 June 2003 event was initialized with the National Center for Environmental Prediction (NCEP) North American Regional Reanalysis (NARR) data with 32 km grid spacing (NCEP, 2005). Boundary conditions were interpolated from the NARR data, which was available at 3-hour intervals.

The outer domain, with 9-km grid resolution, encompassed the continental United States east of the Rocky Mountains. The Kain-Fritsch cumulus parameterization (Kain 2004) was applied in this domain. A nested, convection-allowing, 3-km domain was placed over the Midwestern United States, encompassing the region containing the quad-Doppler analysis (Fig. 1). Both domains had 75 vertical levels, and used the Morrison et al. (2009) microphysics scheme, the Rapid Radiative Transfer Model for General Circulation Models (RRTMG; Iacono et al. 2008) longwave and

shortwave radiation scheme, the Noah Land Surface Model, the Monin-Obukhov (MM5) surface layer scheme, and the YSU planetary boundary layer scheme (Hong et al. 2006).

Sensitivity studies were conducted to examine the impact of various parameterizations. The substitution of the Thompson et al. (2008) microphysics scheme yielded a similar result as the simulation using the Morrison scheme, though with the slight generation of what appeared to be a parallel-stratiform region on the northeast end of the main squall line segment, though observations show that the system was in fact associated with a trailing stratiform structure. An additional test was conducted changing only the land-surface, surface-layer, and planetary boundary layer options to the RUC model, Monin-Obukhov (Eta) scheme, and MYJ scheme (Janjić 1994), respectively. This version of the simulation produced a squall line more representative of the observed structure, though ~2 hours early and displaced to the west by ~200 km.

The simulation was initialized at 0000 on 8 June 2003, and ran with a 15 second time step. The results of this simulation, presented in Chapter 5, are shown to exhibit agreement with observations, and are used to provide insight into the interaction of the squall line with the upper-tropospheric jetstream.

Storm motion was determined in a similar manner as described for the quad-Doppler data, but by using modeled reflectivity as a reference. The resulting storm motion used for storm-relative flow of modeled quantities was from 263º at 15 m s^{-1}.

3. Synoptic Overview

The focus of this study is a frontal squall line which formed in association with a summertime mid-latitude extratropical cyclone. On 5 June 2003, the incipient cyclone began to develop, as a shortwave trough moved southeastward out of Canada into eastern Montana. The shortwave continued into northeastern Nebraska by 1200 on 6 June. A surface pressure trough deepened ahead of the shortwave, forming a surface low pressure center in southern Minnesota. The ensuing extratropical cyclone quickly evolved and the system exhibited a large comma head by 1730 on 8 June (Fig. 5a). At that time, the low had moved to southeastern Wisconsin with a cold front at the surface extending southward through eastern Indiana, and southwestward into Texas as seen in Figs. 5 and 6a. Scattered convection began forming along and ahead of the cold frontal boundary shortly after 1300, with distinct lines of convection organizing along the cyclone's cold front by 1730 (Fig. 5b).

At the time of the data collection, wind speeds at the core of the upper-tropospheric jet exceeded 70 m s^{-1} over southeastern Illinois (Fig. 6b). A disruption in the jet structure is evident in central Ohio, with wind speeds at (40º, -83.5º) and (41.5º, -83º) decreasing by up to 35 m s^{-1}, not associated with the background wind speed gradient, and coincident with the location of the squall line. This interaction is discussed in greater detail in Chapters 4 and 5. The 1600 model sounding at Wilmington, OH (KILN) indicated surface-based CAPE of 1748 J kg^{-1}, with 48 kt 0-7.5 km shear ahead of the approaching cold front and squall line (Fig. 7).

4. Quad-Doppler Analysis of the Squall Line

a. Overview

The segment of the squall line examined with the quad-Doppler analysis consisted of a nearly contiguous line of reflectivity > 40 dBZ, approximately 8 km wide at 1 km above ground level (AGL), along the leading (eastern) edge, with a narrow trailing stratiform region, less than 30 km wide (Fig. 8). Numerous cross-sections, at various orientations relative to the squall line, were analyzed and the cross-section location indicated in Fig. 8 was found to be representative of the structure of the line north and south of that location.

Radar echoes associated with the squall line extended to approximately 10.5 km AGL, with high reflectivities within the eastern 15 km of the system (between 23-38 km in Fig. 9), coincident with the region of greatest upward storm-relative velocities. The beginning of what may be a weak transition zone is evident at 24 km, with the early stages of a trailing stratiform region evident to the west of that location.

b. Jetstream Wind Speeds

Wind speeds at 7.5 km AGL (near jet-level) were predominately in excess of 30 m s^{-1}, with a ribbon of slower speeds roughly centered along the north-south extent of the line (Fig. 10a). An overlay of $w \geq 1$ m s^{-1} reveals that most slower horizontal wind speeds are approximately coincident with the location of greatest updraft velocities (e.g., (39º35', -84º10') and (39º48', -84º)), though the cause of observed decelerations at a number of regions on the northern end of the line (e.g., (40º15', -83º43')) is not readily apparent.

A cross-section through an updraft maximum indicates line-parallel wind speeds ≤ 16 m s^{-1}, chiefly within the confines of the 30 dBZ echo (Fig. 10b), with winds near jet-level at the center

10

of the line (~24 km) up to 14 m s⁻¹ slower than winds at the edges of the line. The intrusion of these slower winds into the jetstream is evident between 14 km and 32 km, with higher wind speeds to either side of, and above the convective line, with a maximum value of ~38 m s⁻¹ at 8 km, and 8 km AGL, as well as at 37 km, and 7 km AGL.

c. Vertical Momentum Transport

The vertical advection of the magnitude of the horizontal wind,

$$-w \frac{d}{dz} |\vec{V}|, \tag{1}$$

was calculated, where w is vertical velocity (positive values are upward), and $\frac{d}{dz} |\vec{V}|$ is the vertical shear of the magnitude of the horizontal wind. A cross-section of this quantity is provided in Fig. 11, where positive values correspond to downward transport of slower wind speeds, or upward transport of faster wind speeds. Negative values correspond to upward transport of slower wind speeds, or downward transport of faster wind speeds. Upward advection of low horizontal wind speeds, and by proxy, low momentum air, dominates the eastern half of the squall line (between ~22-39 km), with the greatest values (> 40 m s⁻²) collocated with the leading line of convection and the region of strongest upward motions. Relatively weaker (5-25 m s⁻²) downward transport of high momentum air is seen in the stratiform region and the far western edge of the system, areas where weak to moderate descent were present.

d. Relative Vertical Vorticity

Vertical vorticity at 7.5 km AGL is shown in Fig. 12, along with 1-7.5 km shear vectors (1 km was the lowest level with widespread recoverable winds). A ribbon of predominately cyclonic (positive) vertical vorticity is present on the eastern half of the squall line, with a ribbon of

anticyclonic (negative) vertical vorticity on the western half. These ribbons of vertical vorticity are aligned with the shear vectors, with only slight deviations observed near updrafts (e.g., 39º35', -84º10') (locations of updrafts indicated in Fig. 10), likely due to modification of jet-level winds observed in those areas.

Following Wakimoto et al. (2015), who found a similar pattern of vertical vorticity at 2.25 km AGL within the 2 June 2003 MCS, an analysis of each term of the scaled vertical vorticity tendency equation was conducted, namely the tilting and stretching terms,

$$\frac{d\zeta}{dt} = -\underbrace{\left(\frac{\partial w}{\partial x}\frac{\partial v}{\partial z} - \frac{\partial w}{\partial y}\frac{\partial u}{\partial z}\right)}_{Tilting} - \underbrace{\zeta\left(\frac{\partial u}{\partial x} + \frac{\partial v}{\partial y}\right)}_{Stretching},$$

(2)

where ζ is defined as

$$\zeta = \frac{\partial v}{\partial x} - \frac{\partial u}{\partial y},$$

(3)

and u, v, and w are the components of velocity. Fig. 13 shows the contribution to the vertical vorticity tendency of stretching and tilting at both 2.5 km and 7.5 km AGL. Tilting of the baroclinically generated horizontal shear by vertical motions within the squall line is the dominant mechanism influencing vertical vorticity, with magnitudes of vorticity tendency exceeding $\pm 8 \times 10^{-6}$ s^{-1} at both levels (Fig. 13b,d). Between the two levels, tilting is most prominent at 7.5 km (Fig. 13d), with positive tendencies generally focused upshear of updrafts, and negative tendencies downshear. The most significant examples of this pattern in Fig. 13d are located directly to the north and south of (39º46', -84º).

Stretching contributes to the vertical vorticity tendency much less at 2.5 km than at 7.5 km (Fig. 13a,c), with values barely surpassing $\pm 4 \times 10^{-6}$ s^{-1} at 2.5 km, likely due to greater divergence

near the top of the squall line. As such, negative tendencies are observed where divergent flow from adjacent updrafts is converging (e.g., Fig. 13c, ~ (39º40', -84º04').

The total vertical vorticity tendency for 2.5 km and 7.5 km, as given by the sum of the stretching and tilting terms in Fig. 13, is shown in Fig. 14. It is difficult to discern any significant differences between the tilting and total terms at each level, with many of the contributions from stretching complementing those from tilting. Negative tendencies in stretching at 7.5 km were found to be the dominant enhancement to the total term, relative to the tilting term alone, particularly in the northern ~10 km of the squall line, and in the region centered at (39º52', -84º53'). Greater convergence in these regions or the preexistence of anticyclonic vertical vorticity would explain these features.

5. WRF Model Analysis of the Squall Line

a. Overview

WRF modeled maximum column reflectivity is provided in Fig. 15, valid at 1730, the time the quad-Doppler analysis was performed. The simulation produced two discreet squall lines by 1730, one in northwestern Ohio and north into Michigan, the other in approximately the same location and orientation as observed (Fig. 5b). The southern line in the simulation presents as a single continuous line through central Kentucky, though the observed line breaks just past the Ohio-Kentucky border, with another line followed by scattered stratiform precipitation located to the south and west. Additionally, the model failed to reproduce the vast majority of precipitation observed in Indiana at this time. These differences aside, the segment of squall line produced in southwestern Ohio, coincident with the quad-Doppler domain, resembles observations in terms of line width, orientation, and relative intensity of the convective line to a satisfactory degree. The shift in surface winds from westerly behind the line in western Kentucky and southern Indiana, to south-southwesterly ahead of the line in eastern Kentucky and south-central Ohio, further supports the notion that this squall line was present along the synoptic cold front.

Similar to the method employed in the quad-Doppler analysis, multiple cross-sections were considered along the length of the modeled squall line, and at various orientations. The general structure of the system along its length is well represented by the cross-section locations defined in Fig. 15. The 900 km cross-section was drawn perpendicular to the squall line and surface cold front, and is intended to provide the broad-scale vertical structure of the system, as seen in Fig. 16. Relative humidity (with respect to water) outlines the location of the squall line centered at 530 km, with values at or nearing saturation from the surface to above 11 km MSL. The position of the synoptic cold front is evident at the surface at the same location, extending upward and westward,

14

as determined by identifying the location of wind shifts behind the squall line, coincident with the upward sloping gradient in relative humidity and contours of potential temperature. The easternmost portion of the cyclone's comma head is apparent in the vertical increase in relative humidity to approximately 60% at the western edge of the cross-section, with the dry slot of the cyclone between this location and the squall line, as seen by a decrease in relative humidity to below 20%.

b. Jetstream Wind Speeds

Fig. 17a shows wind speeds at 300 hPa, similar to Fig. 6b, but using the data from the 3-km WRF simulation. As observed in Fig. 6b, Fig. 17a indicates a considerable disruption in the jetstream structure beginning in north-central Kentucky, and extending northeast through Ohio. Wind speeds of 46 m s^{-1} along the Indiana-Ohio border decrease rapidly towards the convective line (blue contour in Fig. 17a.), ending at a local minimum of 10 m s^{-1} just northeast of the cross-section location in Fig.17a. East of this location, wind speeds increase to ~40 m s^{-1} in southeast Ohio. At the southern end of the squall line, higher wind speeds are observed to be splitting around the system, with a region of wind speeds ranging from ~10-34 m s^{-1} in between, coincident with, and northeast of the main convective line. A number of local minimums in wind speed are observed adjacent to updrafts $\geq$ 1 m s^{-1} (e.g., (38.6º, -84.3º) and (39.2º, -83.8º)), though a number of others (e.g., (40º, -83.3º) and (40.8º, -83º)) are entirely removed from significant vertical motions, and the convective line itself.

The wind speed pattern in Fig. 17a was remarkably similar to the quad-Doppler analysis near jet-level (Fig. 10a), with wind speeds approaching 40 m s^{-1} along the western and eastern edges of the squall line, decreasing to ~12 m s^{-1} at the center of the line, adjacent to many of the updraft cores (e.g., Fig. 10a, (39º35', -84º10') and (39º48', -84º)). The quad-Doppler results also indicate

the presence of local speed minimums absent of any strong vertical motion on the northern end of the squall line (e.g., (40º15', -83º43')), though despite this agreement, an explanation for these outliers is not readily apparent.

Fig. 17b indicates that nearly the entire vertical depth of the squall line is associated with line-parallel wind speeds of 16 m s^{-1} or less. These slower wind speeds are approximately contained within, and immediately adjacent to the location of the 30 dBZ echo, with a minimum wind speed of 8 m s^{-1} near jet level at 30 km, ~8.5 km MSL. The maximum wind speeds splitting around the convective line were ~40 m s^{-1} at 9 km MSL on the western edge of the cross-section, as well as 32 m s^{-1} at 6.5 km MSL on the eastern edge. The vertical structure of wind speeds from the simulation (Fig. 17b) is in excellent agreement with those observed in the quad-Doppler analysis (Fig. 10b), with only minor variations in magnitude ($\sim \pm 5$ m s^{-1}) and location of the various features.

c. Vertical Momentum Transport

Absolute momentum was calculated from the WRF simulation and analyzed in a vertical cross-section normal to the convective line (Fig. 18), where absolute momentum is defined as

$$M_{abs} = v + fx, \tag{4}$$

where v is the wind velocity perpendicular to the cross-section, f is the coriolis parameter at the middle of the cross-section, and x is the distance along the cross-section. Values approaching 35 m s^{-1} are present to either side and above the convective core of the storm, with an intrusion of relatively low momentum air of less than 5 m s^{-1} from the boundary layer (at 37 km, below ~3 km MSL) being transported upward via the convective updraft. At 30 km, and 9 km MSL, absolute momentum reaches a local minimum of -1 m s^{-1}. The region of negative values below 2 km MSL and between 0 km and 36 km is evidence of the wind direction reversal (relative to the

cross-section), and is indicative of flow within the system generated cold pool and/or behind the surface cold front.

While Fig. 18, and Fig. 11 from the quad-Doppler analysis depict different variables, both are intended to provide a sense of the momentum transport within the squall line. Both strongly indicate that vertical momentum transport was maximized on the eastern half of the squall line, effectively modifying and decreasing the momentum within the jetstream.

d. Relative Vertical Vorticity

Vertical vorticity at 9 km MSL (Fig. 19) indicates similar ribbons of cyclonic and anticyclonic vorticity to those observed in the quad-Doppler analysis (Fig. 12). In both the simulation and quad-Doppler analysis, these ribbons are aligned with the wind shear vectors. Magnitudes of vertical vorticity were approximately half of those observed in the quad-Doppler simulation, a difference very likely attributed to the lower resolution of the 3-km simulation, relative to the 1-km quad-Doppler observations. While still producing a pattern of predominately anticyclonic vertical vorticity on the back (western) half of the line, and cyclonic vertical vorticity on the front (eastern) half as in the quad-Doppler analysis, the simulated vertical vorticity field is notably more chaotic south of 40º, with segments of the ribbons appearing to break and rotate slightly to the east, while remaining coupled to ribbons of the opposite sign (e.g., the local couplet centered at (38.1º, -84.2º)). This tendency was observed to continue through at least 1900 (not shown), with discrete couplets of anticyclonic and cyclonic vertical vorticity rotating with the 0-6 km shear vector south of 39.5º, while the ribbons of vertical vorticity in the region of the line north of 39.5º maintained a squall-line-parallel orientation.

The tilting and stretching terms of the vertical vorticity tendency equation (2) were calculated from the simulation and are shown in Fig. 20. In agreement with the quad-Doppler analysis

(Fig. 13d), the tilting term appears the most influential in the tendency of vertical vorticity when compared to stretching, achieving magnitudes in excess of $\pm 4 \times 10^{-6}$ s^{-1} in many locations along the squall line (Fig. 20b). These values are about half of the magnitude observed in the quad-Doppler analysis, consistent with the lower relative vertical vorticity observed in the simulation as discussed above. Most updraft cores are associated with a couplet of approximately equal magnitude cyclonic and anticyclonic tendency (e.g., (38.4º, -84.4º) and (39º, -83.9º)), aligned to the local shear vector. Similar couplets are also observed in the absence of any obvious forcing (i.e., an updraft), particularly along the east and west flanks of the 30 dBZ contour in Fig. 20b. A similar pattern was noted in the quad-Doppler analysis, though these anomalous couplets were only observed on the northeast tip of the squall line (Fig. 13d).

Regions of the greatest stretching were found to be focused most notably on the upshear side of updraft cores, with values nearing -4×10^{-6} s^{-1} (e.g., Fig. 20a, (38.5º, -84.4º) and (39.3º, -83.8º)). This pattern is comparable to that observed in the quad-Doppler stretching term (Fig. 13c), though as previously alluded to, of a smaller magnitude by about half.

The total vertical vorticity tendency (Fig. 21) was computed by adding the tilting and stretching terms. The similarity of this field to the isolated tilting term (Fig. 20b) provides further evidence that tilting of the baroclinically-induced horizontal shear vorticity was the primary means of vertical vorticity generation in this system. Of note, are the regions with a higher magnitude of anticyclonic tendency, when compared with the cyclonic counterpart (e.g., (38.5º, -84.4º)). While such mismatched pairs are not dominant in this analysis, they are numerous enough to suggest an overall anticyclonic tendency where observed.

The axis between the couplets in the total vertical vorticity tendency field is aligned nearly perpendicular to the squall line in some locations south of 39.2º (e.g., (38.5º, -84.4º)), which may

help to account for the tendency of the couplets in this region to rotate into a more line-normal orientation, as was observed in the vertical vorticity field later in the simulation.

e. Pressure Perturbations

Pressure perturbations were plotted at 7.5 km MSL (Fig. 22) in an effort to determine the applicability of obstacle-flow to this study. Pressure perturbations were found to align quite well with the 0-7.5 km shear vectors, with positive perturbations exceeding 0.7 hPa on the upshear side of many updraft cores (e.g., (38.5º, -84.4º), and negative pressure perturbations of the same magnitude on the downshear side (e.g., (38.6º, -84.05º)). As per Rotunno and Klemp (1982), this pattern is not indicative of obstacle-flow, as the pressure perturbations would instead be aligned to the storm-relative wind vector. Therefore, obstacle-flow theory is not considered to be appropriate for describing the observed flow patterns in the present system.

6. Discussion

The nature of, and possible feedbacks associated with the interactions presented in the previous chapters will be discussed in terms of the jetstream wind speeds, the applicability of obstacle-flow with a consideration of induced pressure perturbations, vertical momentum transport, along with relative vertical vorticity ribbons and the contributions to the vertical vorticity tendency.

The upper-tropospheric jetstream present on 8 June 2003 was associated with a deep shortwave trough, and had maximum wind speeds exceeding 70 m s^{-1} at its core. The squall line, which formed along the surface cold-frontal boundary, transported lower-tropospheric air into the upper-tropospheric jetstream at a location where jetstream winds were approaching 50 m s^{-1}. Quad-Doppler and model analyses both indicate a disturbance of the jet structure causing winds of higher speeds to split around the convective line. Regions within the squall line, particularly areas coincident with, and downstream of positive vertical velocities, were associated with horizontal wind speeds on the order of 18 m s^{-1} or less, suggesting that the convective system was responsible for locally reducing jet-level winds by more than 30 m s^{-1}. At first glance, this pattern seems to be suggestive of obstacle-flow, where the convective updrafts would act as solid bodies and force higher winds to split around them.

If the convective updrafts were to behave as solid cylinders, any flow encountering these updrafts would presumably divert around them, and leave the atmospheric state within the updrafts relatively unchanged. Rotunno and Klemp (1982) challenged this notion and suggested that a convective updraft is rather porous, and thus susceptible to influence by its environment with flow into and out of the column, and is consequently incapable of acting as a truly *solid* cylinder. They showed that the pressure gradient induced across an updraft is aligned with the environmental shear vector, and not the storm-relative wind vector as would occur if the updraft acted as an

obstacle. Indeed, the pressure perturbation field at 7.5 km MSL seen in Fig. 22 is clearly aligned with the 0-7.5 km environmental shear, suggesting that the obstacle-flow model does not account for the flow pattern observed in this study.

A more likely explanation for the apparent deceleration observed in the upper-tropospheric jetstream is the vertical transport of momentum via convective updrafts within the squall line. Vertical advection of the horizontal wind by the convective updraft was shown in Fig. 11, and provided a proxy for vertical momentum transport in the absence of pressure and density fields from the quad-Doppler analysis. Values exceeding -40 m s^{-2} were observed within the convective updraft, suggesting strong upward transport of relatively slow horizontal winds, and by proxy, low momentum air. Simulated absolute momentum confirmed these results, indicating low momentum air from the boundary layer was drawn upward within the convective updraft, penetrating the upper-tropospheric jetstream. Values of absolute momentum were locally lowered within the jetstream by as much as 40 m s^{-1}, and even changed direction near jet-level, relative to the analyzed cross-section.

In addition to momentum transport from the boundary layer, the convective updraft accomplishes vertical vorticity generation through the tilting and stretching of baroclinically induced horizontal shear vorticity. When computed from both the quad-Doppler analysis and the WRF simulation, both terms of the scaled vertical vorticity tendency equation were found to contribute to the observed and simulated vertical vorticity pattern in the upper-troposphere, though tilting was by far the most dominant of the two terms. Couplets of cyclonic and anticyclonic vertical vorticity tendencies were found to be aligned parallel to the shear vectors, and across updraft cores within the squall line, due primarily to tilting induced via the strong upward motions in these regions.

21

Horizontal vorticity vectors were plotted relative to the tilting tendencies (not shown) at 1600, prior to the passage of the squall line to ensure a relatively undisturbed environment. These vectors were aligned normal to the axis of many of the tilting tendency couplets observed at 1730 in the simulation. This suggests that the vertical motion in the updrafts tilted these horizontal vorticity vectors into the vertical, creating the observed tilting contributions to vertical vorticity.

The resulting vertical vorticity field was organized in ribbons of anticyclonic and cyclonic vertical vorticity, primarily focused on the western and eastern halves of the convective line, respectively. This pattern is consistent with that found by Wakimoto et al. (2015), though their analysis was focused in the lower levels. It should be noted that the organization and magnitude of the tilting and shearing terms at 2.5 km AGL in the present study (Fig. 13a,b) are comparable in magnitude and orientation relative to the convective line, to those found by Wakimoto et al. (2015).

The total vertical vorticity tendency couplets were aligned at an angle to the squall line, particularly in the southern half of the line. This orientation is suggestive of a continual breakdown of the line-parallel ribbon structure observed. The previously discussed forward simulation of vertical vorticity to 1900 suggested this was indeed the case, as the cyclonic and anticyclonic couplets of vertical vorticity broke from the original line-parallel orientation, forming discrete couplets.

As Eagleman and Lin (1977) suggested, counter-rotating vertical vorticity couplets can act to decelerate opposing ambient flow between the couplets, along with diverting flow around the couplet, in a manner that may *resemble* an obstacle-flow pattern. Given the observed deceleration of winds at jet-level along the center of the squall line, coupled with the orientation of counter-rotating couplets of vertical vorticity straddling this region of slower winds, it can be

concluded that the couplets were acting to directly oppose the flow of the jetstream, while also diverting higher speed flow to either side of the squall line. This, along with the vertical advection of low momentum air from the boundary layer, combined to produce the observed local minimums in wind speed within the jet, along with the broad scale deceleration surrounding the main convective line.

7. Conclusions

This study examined the interactions between a squall line, which formed along a surface cold front associated with a summertime mid-latitude extratropical cyclone, and an upper-tropospheric jetstream. These interactions were identified using an airborne quad-Doppler analysis of data collected on 8 June 2003 with the NOAA Tail Doppler Radar aboard the NOAA P-3, and the Electra Doppler Radar aboard the NRL P-3. The 8 June observation period was conducted as a part of the Bow Echo and Mesoscale Convective Vortex Experiment. The quad-Doppler analysis was combined with a Weather Research and Forecasting model simulation of the event, to provide complementary analyses through larger domains, longer time periods of evolution, and to allow for more process studies.

The key findings of this study are as follows:

1) The vertical transport of low momentum air from the boundary layer via convective updrafts acted to locally decelerate flow within the upper-tropospheric jetstream located directly above the squall line.

2) The deceleration of the upper-tropospheric flow coincident with the squall line, coupled with the diversion of faster flow around the line, is reminiscent of flow around a solid obstacle. However, jet-level pressure perturbations across the updrafts were found to be aligned with the environmental shear vector, not the storm-relative wind vector as would occur with obstacle-flow.

3) Ribbons of anticyclonic and cyclonic relative vertical vorticity at jet-level were observed on the western and eastern halves of the squall line, respectively. An analysis of the scaled vertical vorticity tendency equation revealed tilting of baroclinically

24

induced horizontal shear vorticity by the convective updrafts to be the primary source of this observed pattern.

4) The counter-rotating vertical vorticity ribbons likely acted to cause further deceleration of the jetstream at the center of squall line by directly opposing jet-level flow, and by encouraging the diversion of faster flow to either side of the line.

The frontal squall line presented herein was not particularly extraordinary relative to similar systems frequently observed in association with mid-latitude cyclones. However, there have been no documented studies exploring the interactions of such systems with upper-tropospheric jetstreams. It is expected that jetstream interruption and deceleration is quite common when collocated with squall lines, or any convective storm consisting of sufficient updraft magnitude to both transport low momentum air from the boundary layer to jet-level, and to produce properly aligned couplets of vertical vorticity at jet-level.

Further work is needed to determine the long term impacts of the observed squall line and jetstream interaction, though results from the WRF simulation suggest the local deceleration within the jet is temporary, eventually presenting as turbulent eddies at 300 hPa on the far eastern edge of the jetstream as the squall line outpaces the synoptic-scale trough.

Tables

	NOAA TDR	ELDORA
Antenna rotation rate (° s^{-1})	60	140
No. of samples	32	24
Pulse repetition frequency (Hz)	2133/3200	2000/2500
Gate length (m)	150	150
Sweep angle resolution (°)	0.75	1.4
Fore tilt (°)	19.25	18.5
Aft tilt (°)	19.48	18.5
Along-track resolution (m)	1200	300
Max range (km)	46.8	60
Max unambiguous velocity (m s^{-1})	51.5	77.2

Table 1. Scanning parameters for the NOAA TDR and ELDORA airborne radars.

Figures
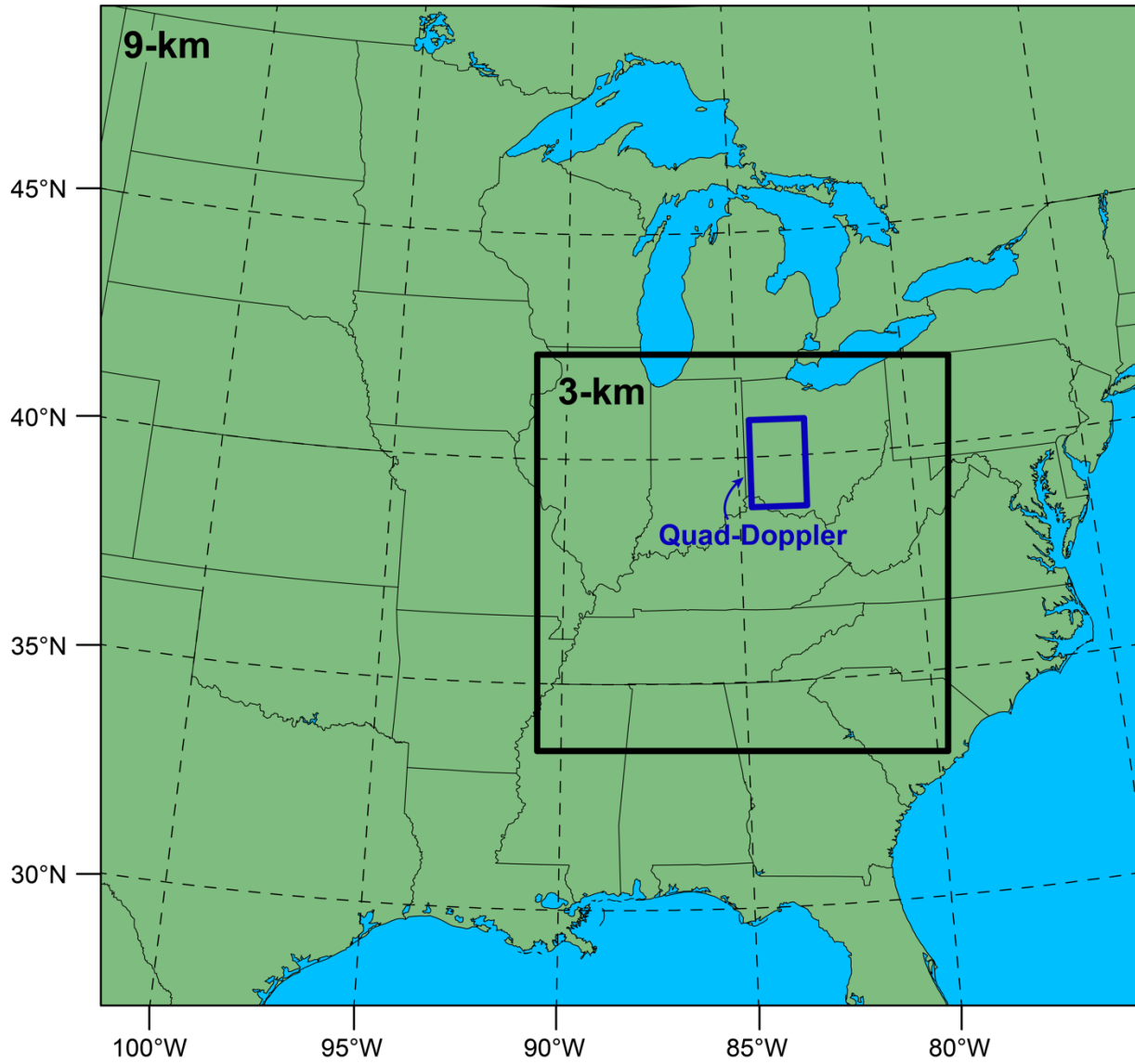
Fig. 1. Location of quad-Doppler domain indicated by the dark blue rectangle. Parent domain of WRF simulation (9-km grid spacing) given by frame of figure. Nested domain of WRF simulation (3-km grid spacing) given by black rectangle.
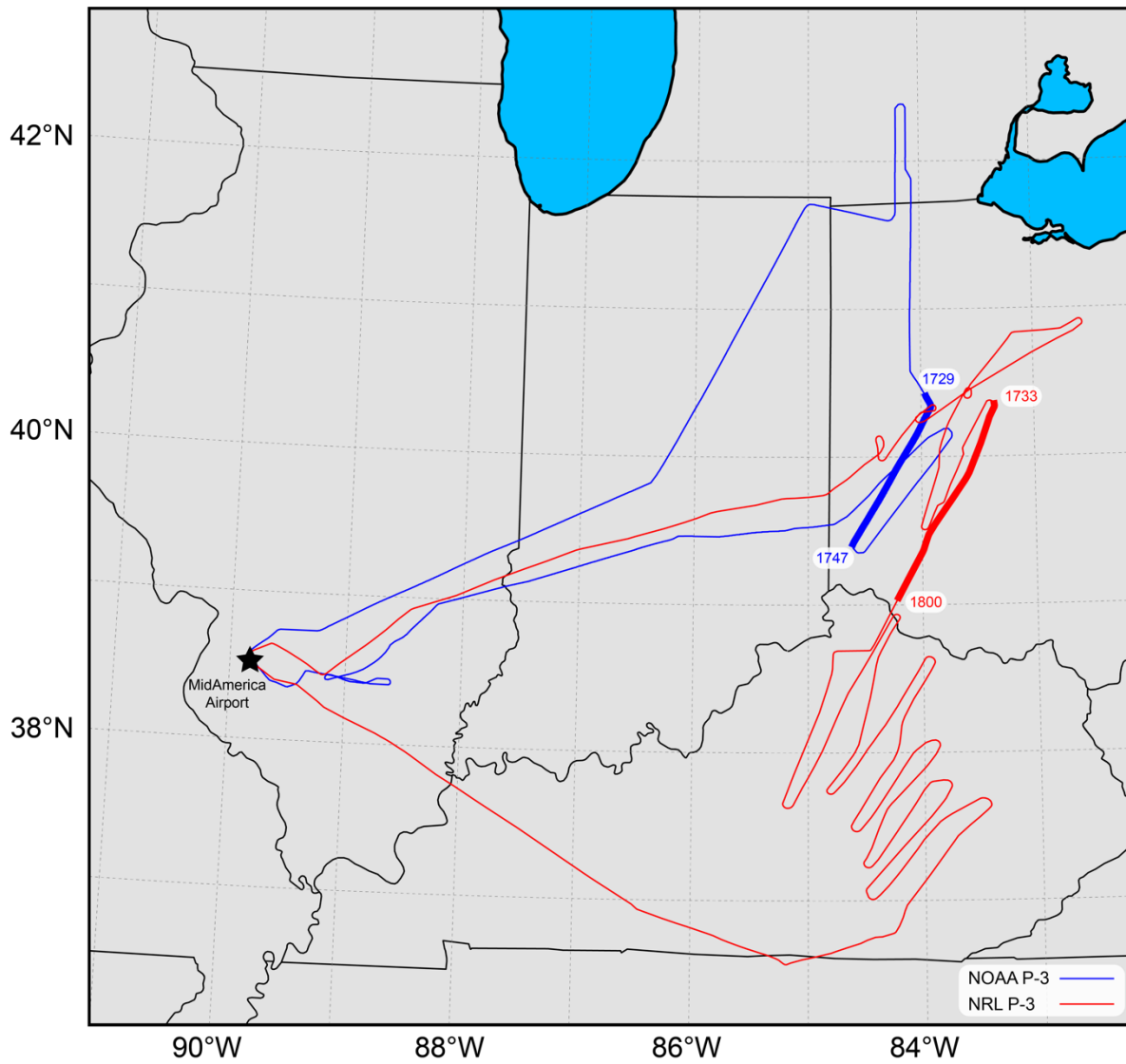
Fig. 2. Flight tracks of the NOAA P-3 (blue line) and NRL P-3 (red line) on 8 June 2003. Bold portions of the flight tracks indicate the location of the quad-Doppler leg. Times (UTC) are given for the beginning and end of each of these legs.
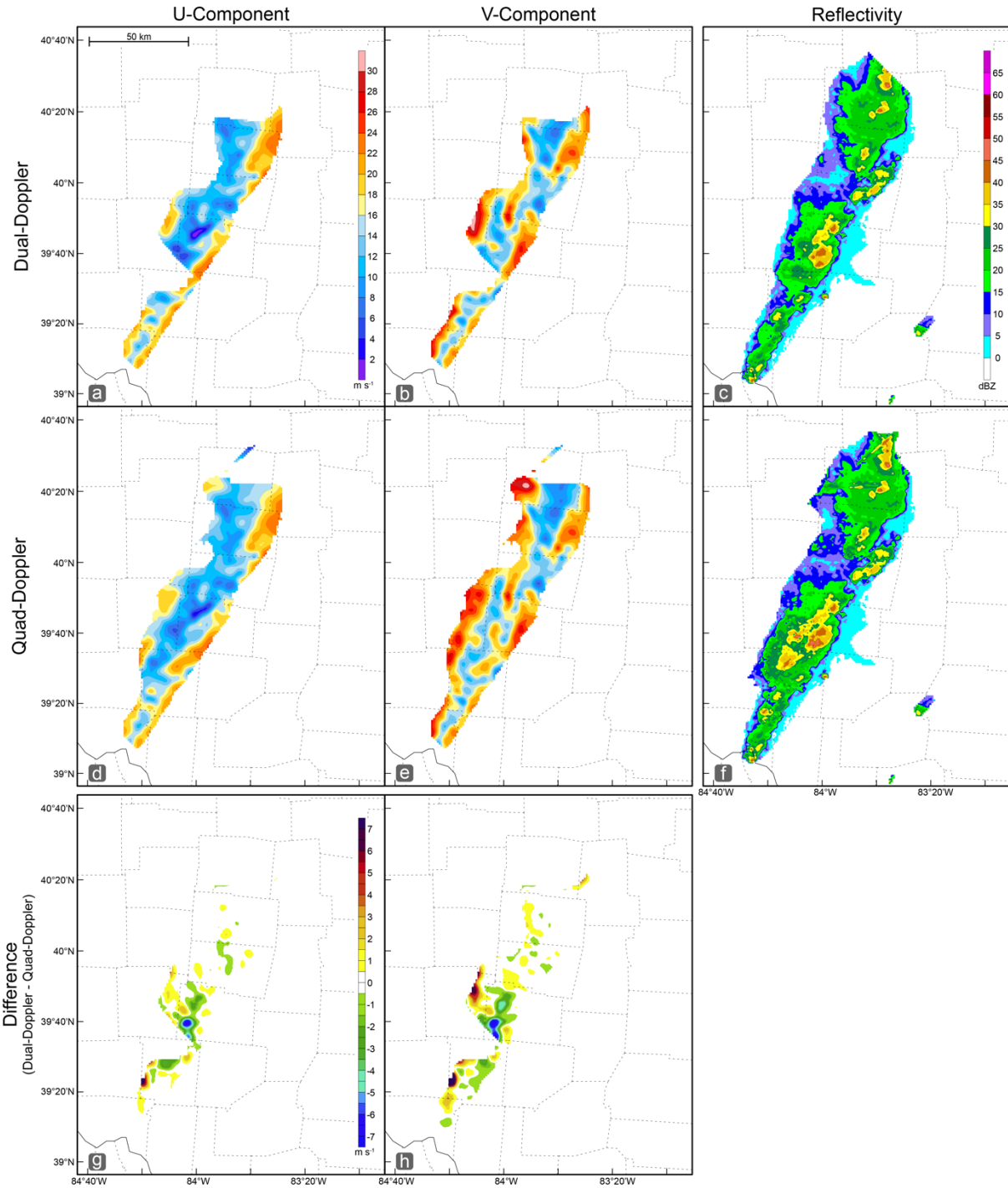
Fig. 3. Comparisons between dual-Doppler and quad-Doppler analyses of the squall line at 6 km AGL, at 1733 8 June 2003. Dual-Doppler determined (a) u-component of the wind (m s^{-1}), (b) v-component of the wind (m s^{-1}), and (c) reflectivity (dBZ) are given along with quad-Doppler determined (d) u-component of the wind (m s^{-1}), (e) v-component of the wind (m s^{-1}), and (f) reflectivity (dBZ). Differences in the u- and v-components of the wind (m s^{-1}), given by (dual-Doppler – quad-Doppler), in (g) and (h), respectively. Color scale in (a) also applies to panels (b), (d), and (e). Color scale in (c) also applies to panel (f). Color scale in (g) also applies to panel (h).
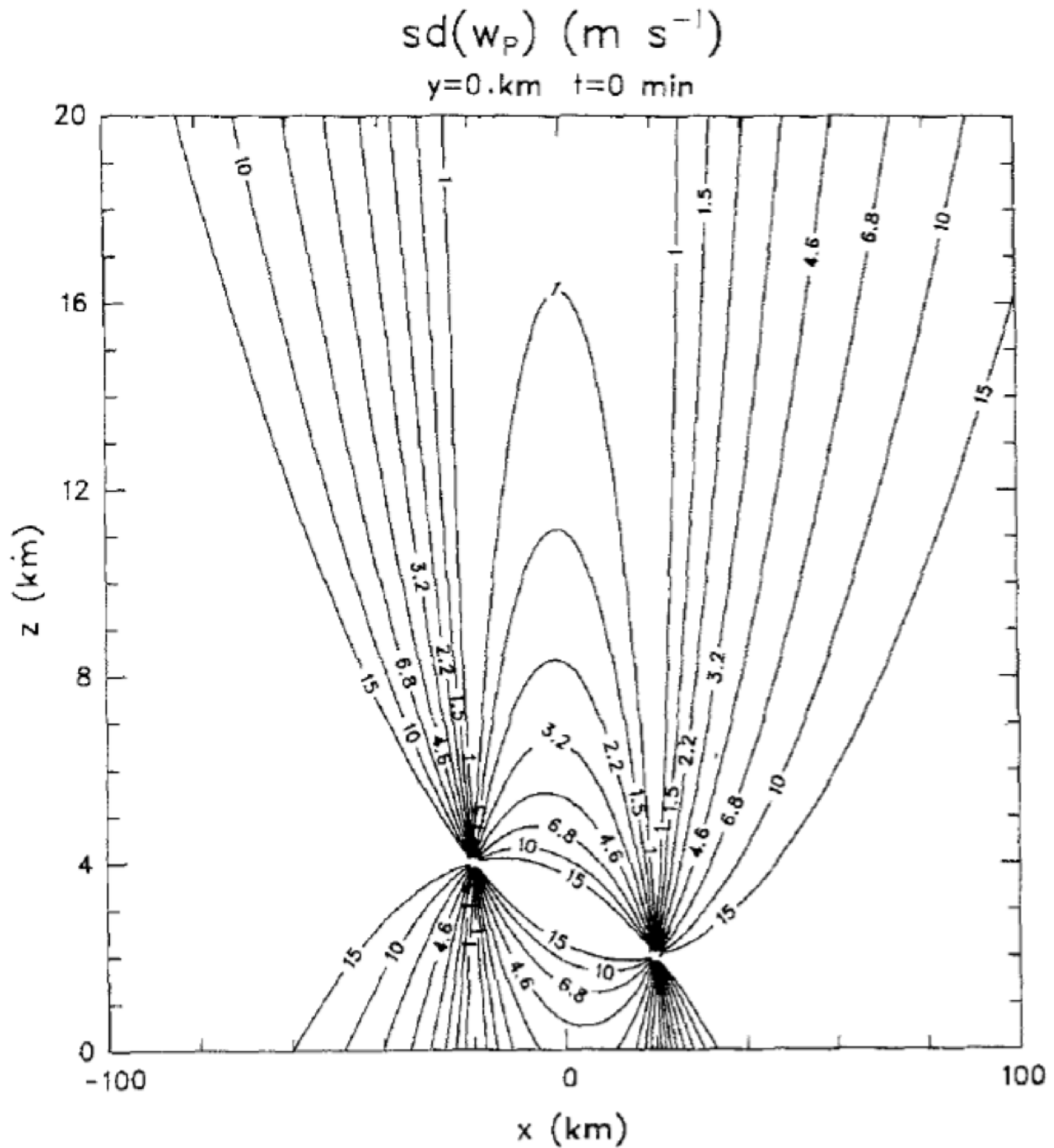
Fig. 4.[1] Cross-section indicating the normalized standard deviation of vertical velocity σ_{wp} (m s^{-1}) relative to the overdetermined triple Doppler equation solution (Jorgensen et al. 1996). The cross-section is drawn perpendicular to aircraft motion. Location of echo-top in the present study was located at ~10.5 km AGL. The location of the NOAA TDR is at -20 km, and 4 km AGL (4.4 km AGL in the present study) and ELDORA was located at +20 km, and 2 km AGL (2.2 km in the present study).

---

[1] Reprinted with permission, from (Jorgensen et al. 1996; their Fig. 7).

30
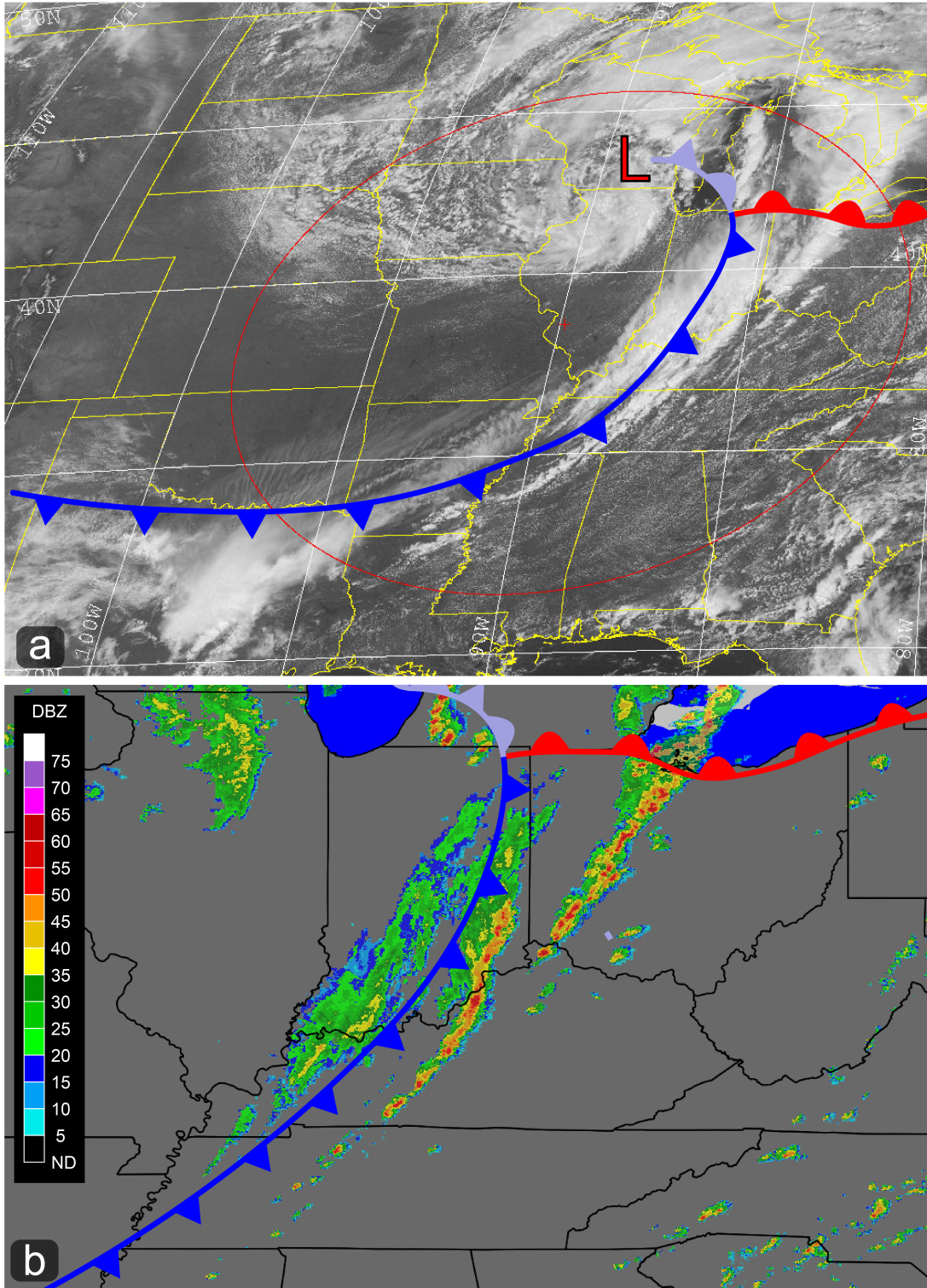
Fig. 5. Surface low pressure center and subjectively analyzed surface fronts for 8 June 2003 overlaid on (a) GOES-12 2 km visible satellite imagery, valid at 1733, with a red ring indicating the extent of BAMEX domain, and (b) WSR-88D base reflectivity composite, valid at 1735.
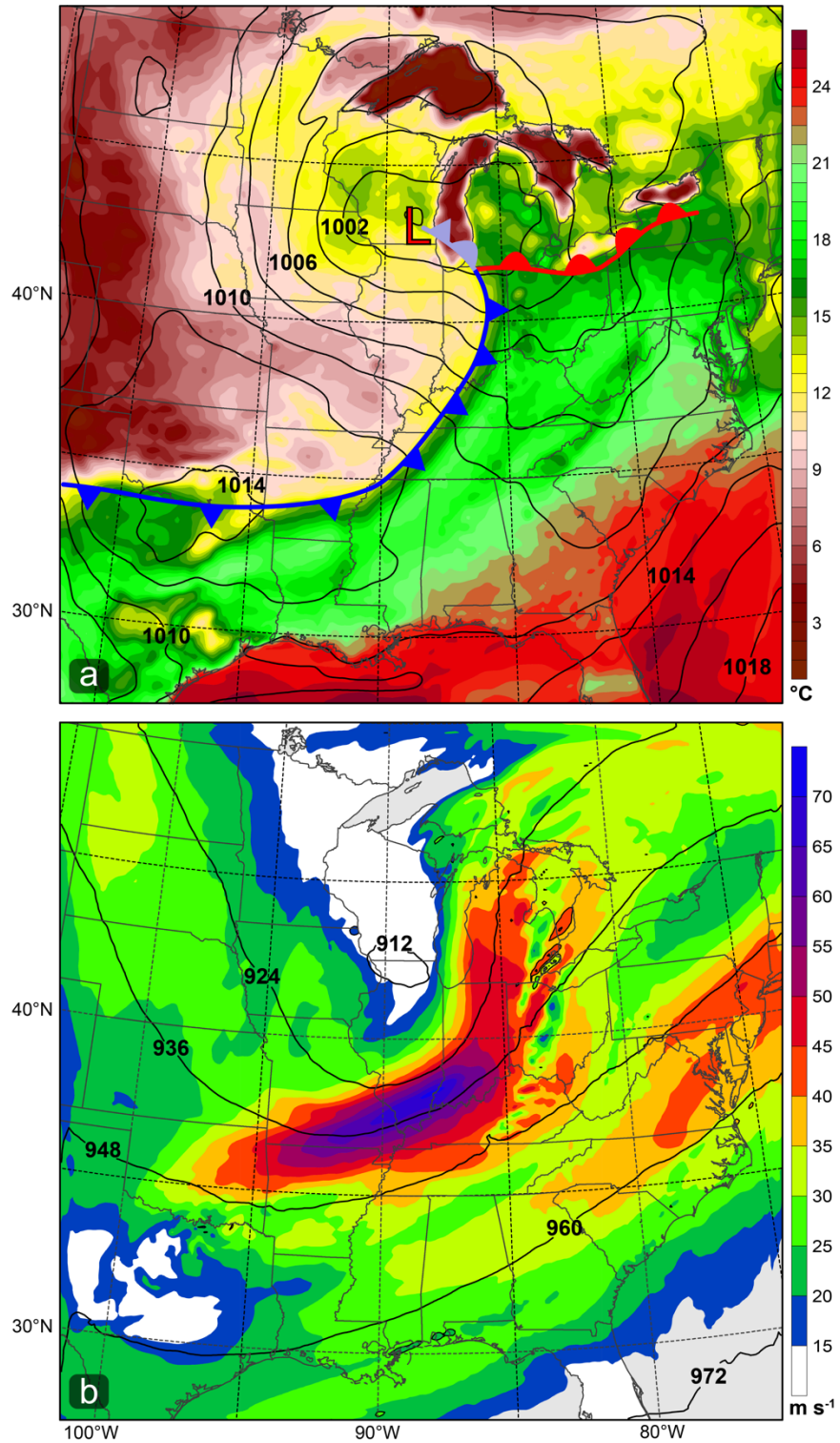
Fig. 6. Synoptic-scale overview of the 8 June 2003 extratropical cyclone. WRF model output valid at 1730 of (a) mean sea-level pressure (black contours; every 2 hPa) and surface dewpoint temperature (filled; ºC), and (b) 300 hPa geopotential height (black contours; every 12 dam) and wind speed (filled; m s^{-1}).
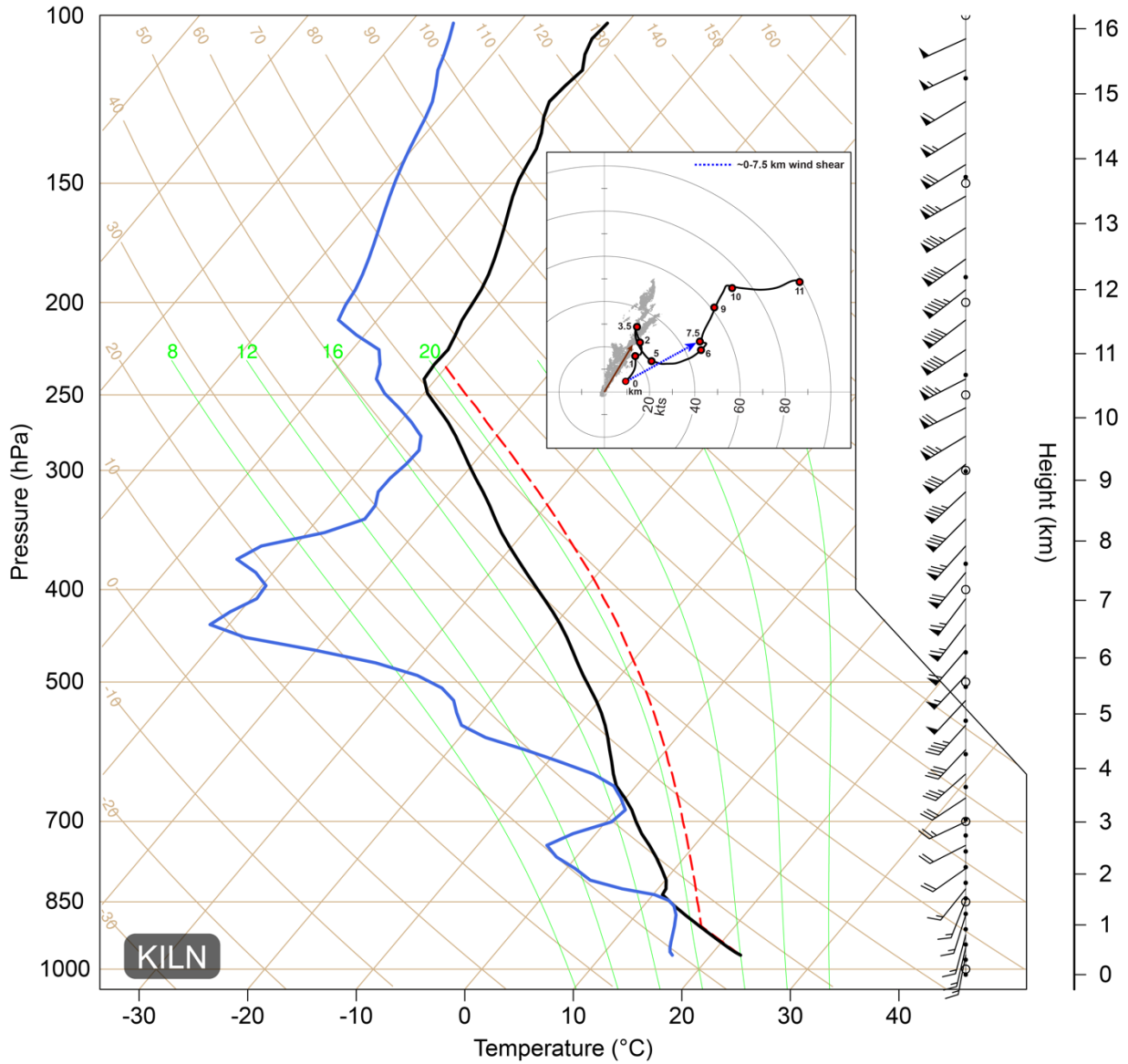
Fig. 7. Atmospheric sounding from the WRF model simulation, initialized at Wilmington, OH (KILN) at 1600. Black line indicates temperature (ºC), solid blue line indicates dewpoint temperature (ºC), and red dashed line represents the parcel trajectory. Winds at various altitudes are provided on the right (knots). Hodograph indicates wind speeds (knots) with height (km). 0-7.5 km wind shear given by dashed blue arrow, and storm motion vector (based on observations) given by dark red arrow. Grey shading indicates > 30 dBZ reflectivity from the quad-Doppler analysis, provided as a reference for squall line orientation.
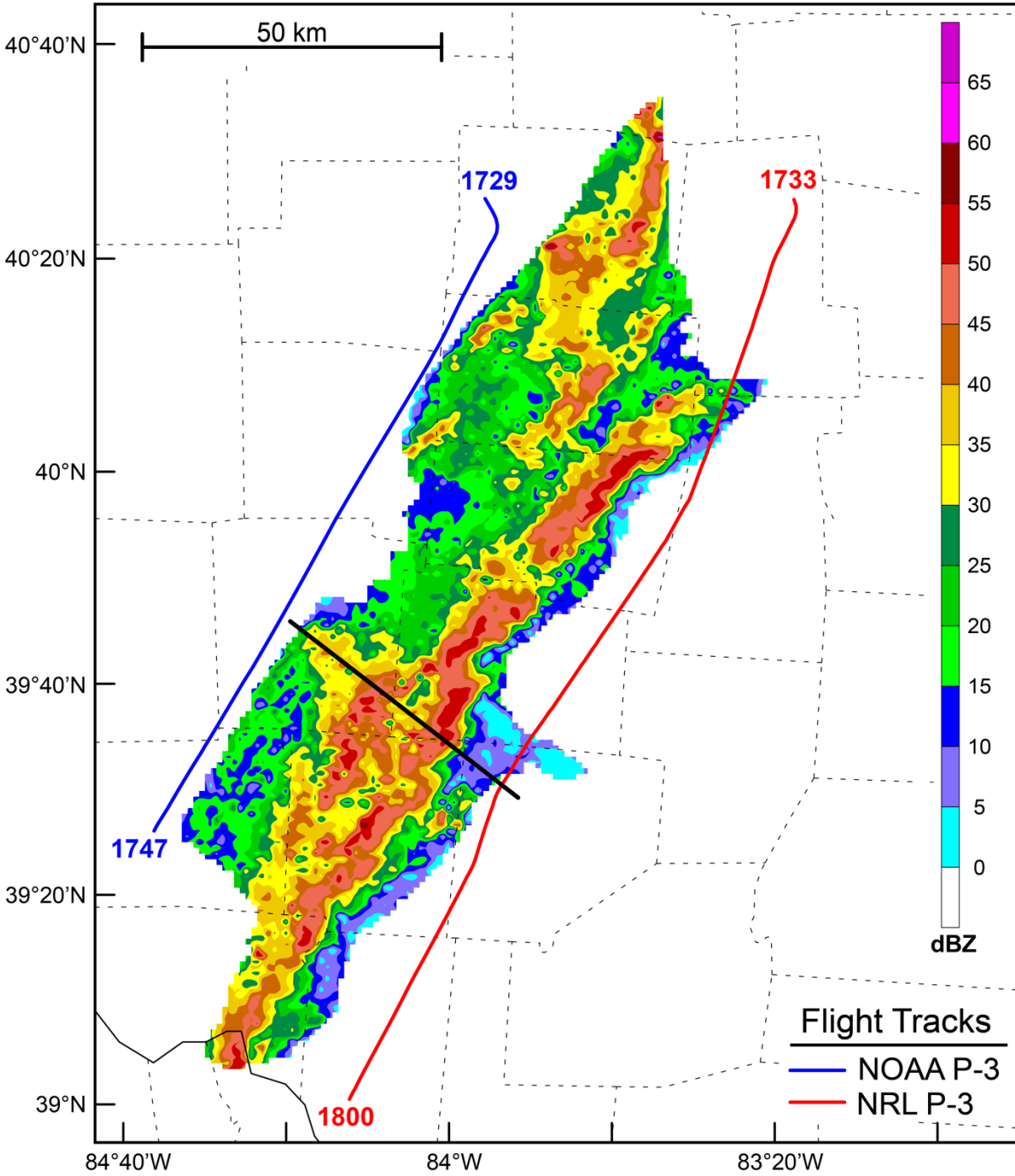
Fig. 8. Quad-Doppler analysis of reflectivity (dBZ) at 1 km AGL, valid at 1733 8 June 2003. Flight tracks of the NOAA P-3, and NRL P-3 aircraft are given by the blue and red lines, respectively, with analysis start and end times given for each. Black line indicates location of quad-Doppler cross-sections in Figs. 9, 10, and 11.
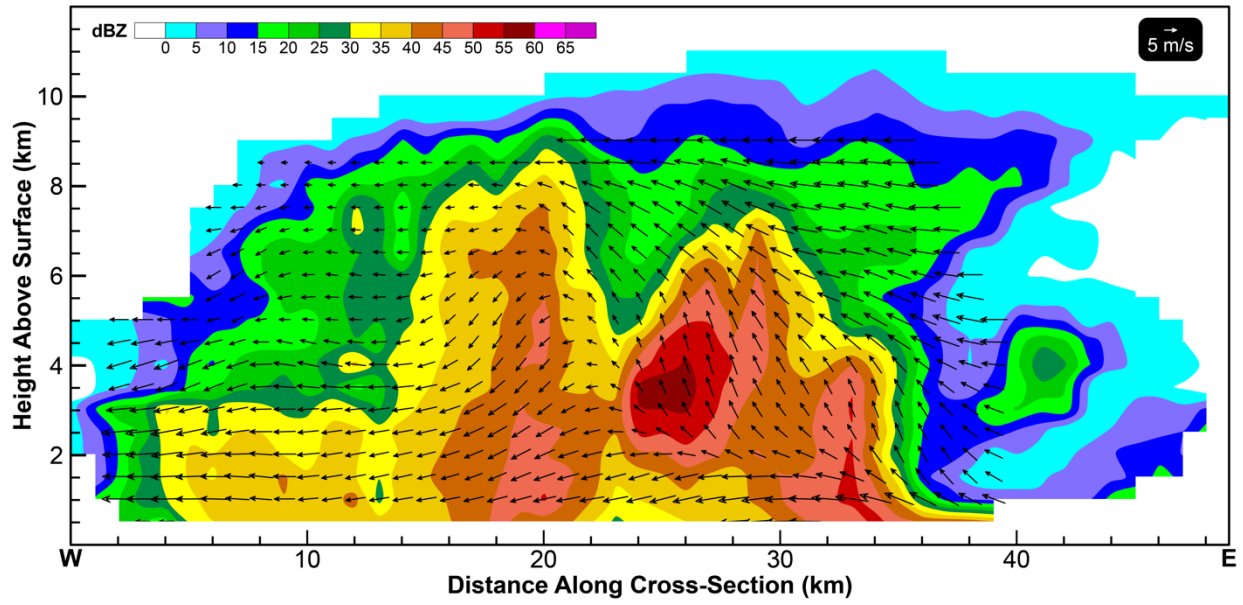
Fig. 9. Cross-section of quad-Doppler analysis of reflectivity (dBZ) (location defined in Fig. 8), and storm-relative winds (m s^{-1}) rotated to the plane of the cross-section, valid at 1733 8 June 2003.
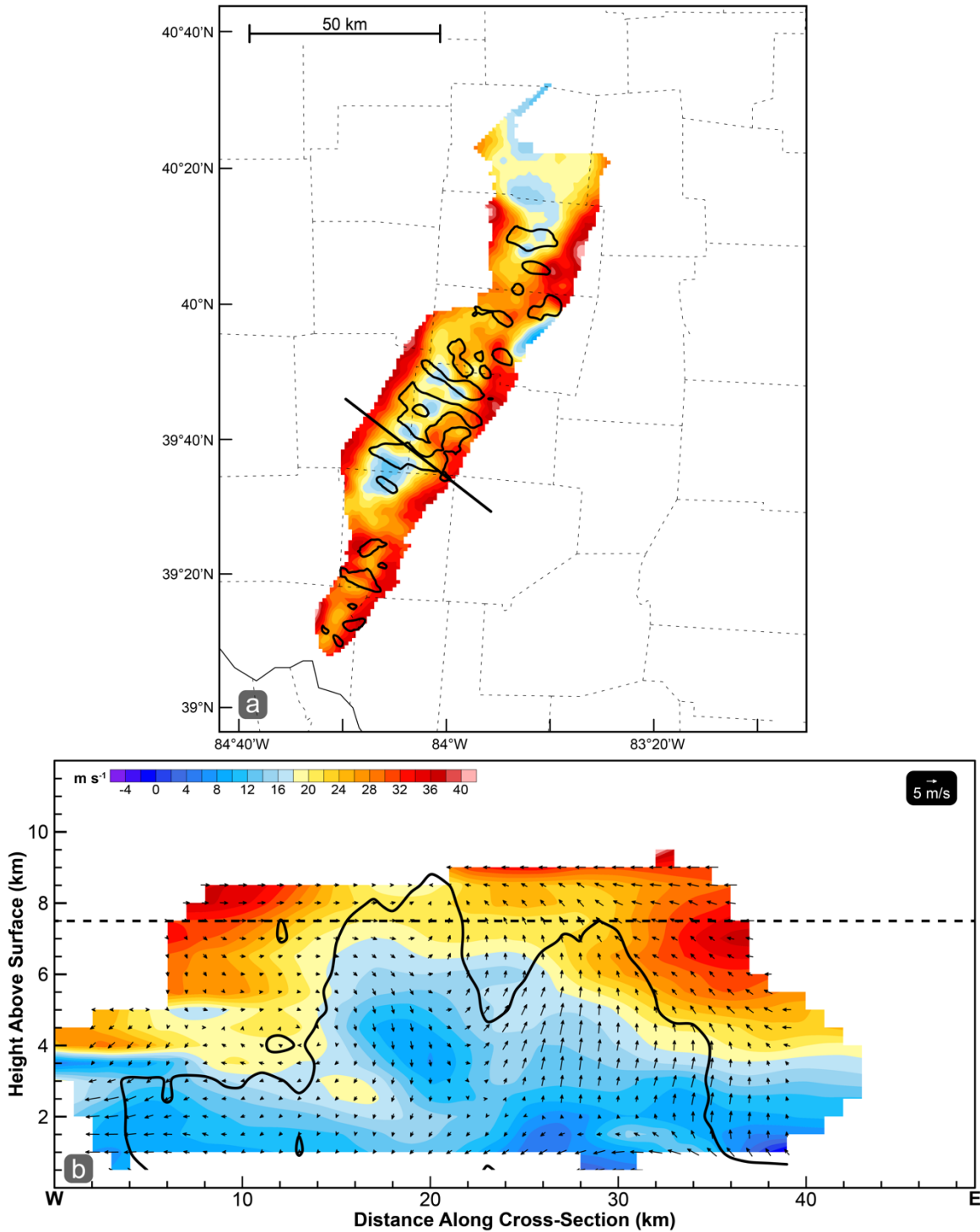
Fig. 10. Quad-Doppler analysis, valid at 1733 8 June 2003, of (a) wind speed (filled; m s^{-1}), $w \geq 1$ m s^{-1} at 7.5 km AGL (black contours), and location of cross-section in (b) (black line), and (b) cross-section of the component of the wind parallel to the squall line (filled; m s^{-1}, positive into page), wind vectors in the plane of the cross-section (m s^{-1}), location of reflectivity ≥ 30 dBZ (solid black contours), and the height of the 7.5 km wind speeds in (a) (dashed black line). Color scale in (b) also applies to (a).
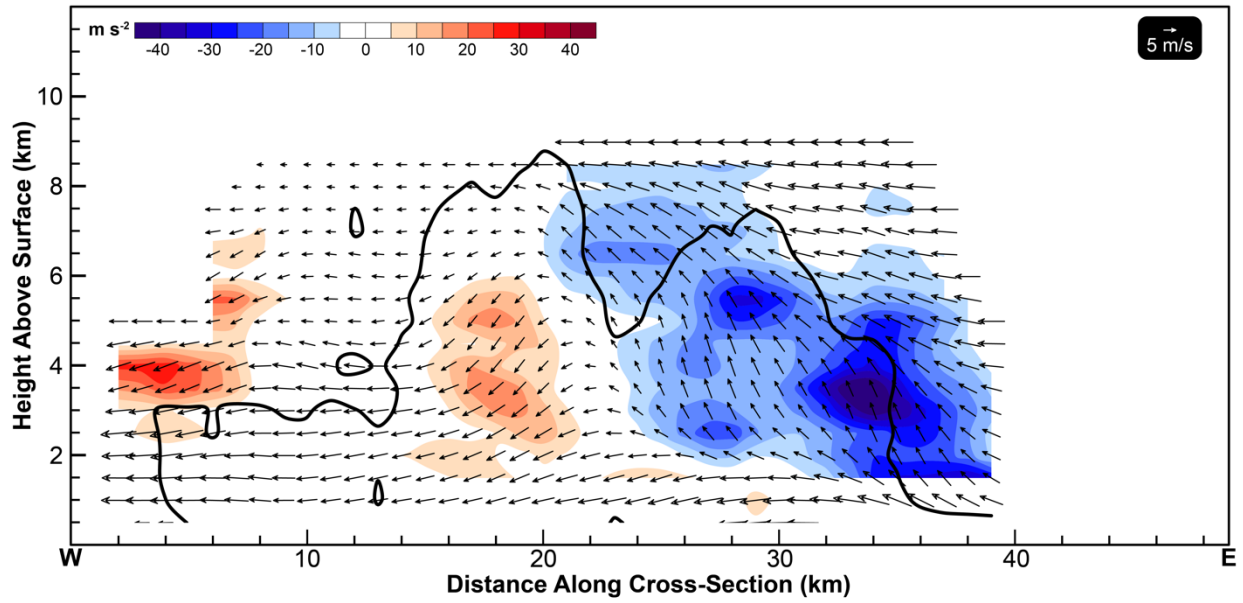
36

Fig. 11. Cross-section from the quad-Doppler analysis (location defined in Fig. 8) of the vertical advection of the magnitude of the horizontal wind (filled; m s^{-2}), as defined in Equation 1, valid at 1733 8 June 2003. Wind vectors are storm-relative (m s^{-1}) and in the plane of the cross-section. Black contours indicate the location of reflectivity ≥ 30 dBZ.
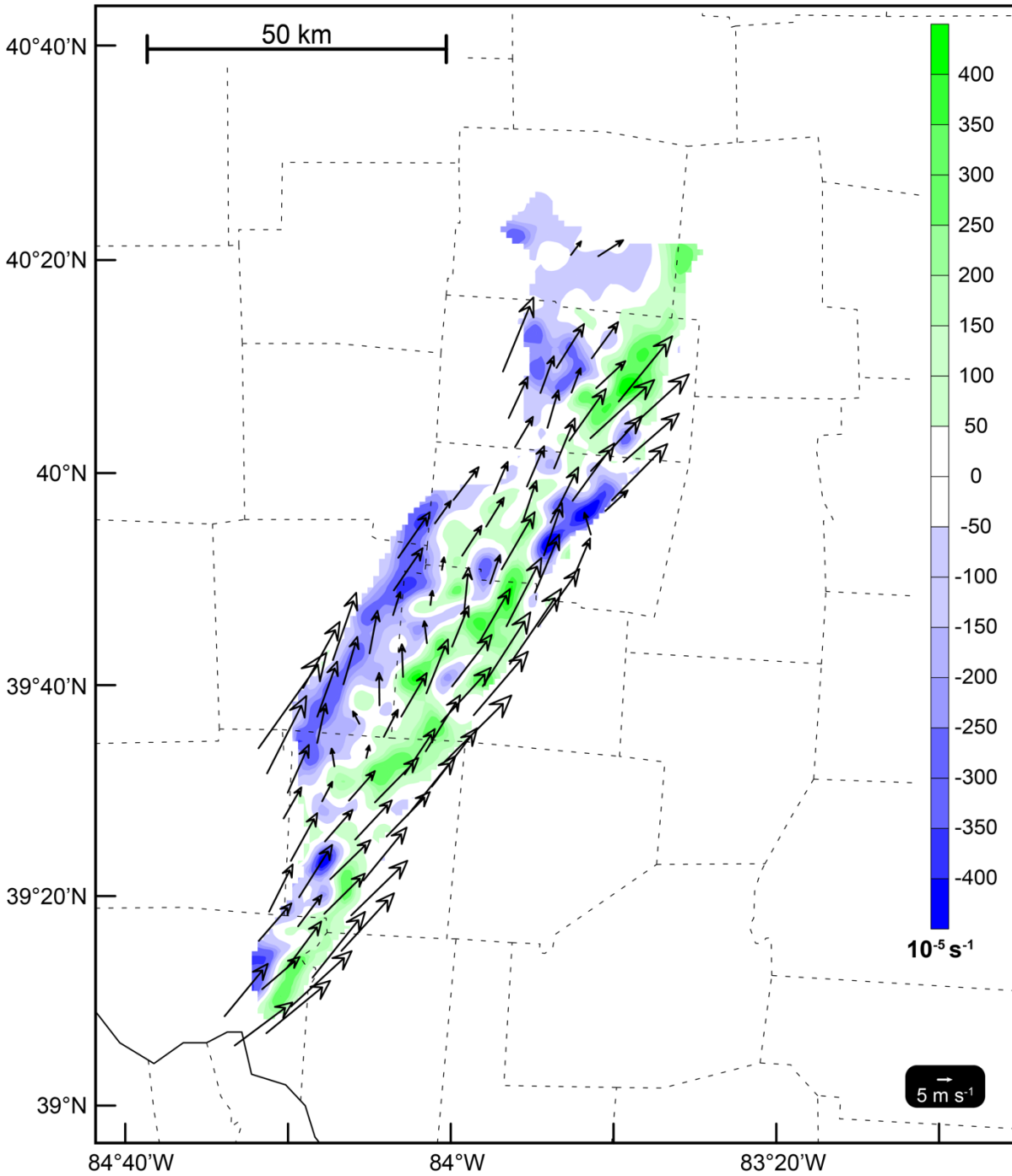
Fig. 12. Vertical vorticity (10^{-5} s^{-1}) at 7.5 km AGL, derived from the quad-Doppler analysis, valid at 1733 8 June 2003. Positive values correspond to cyclonic vertical vorticity and negative values correspond to anticyclonic vertical vorticity. Wind vectors indicate 1-7.5 km wind shear (m s^{-1}).
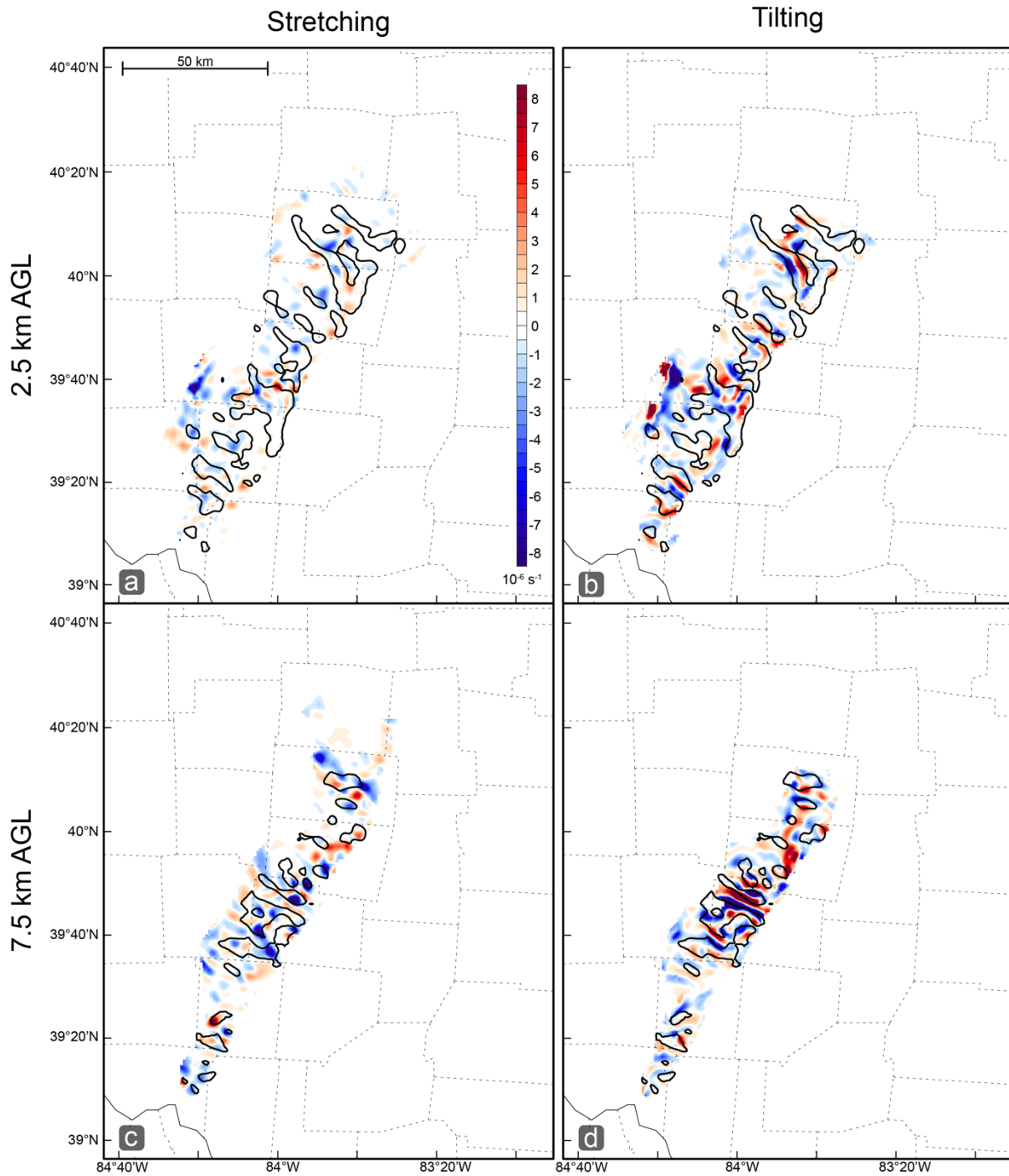
Fig. 13. Quad-Doppler analysis valid at 1733 8 June 2003 of the components of the scaled vertical vorticity tendency equation (2), each with units of 10^{-6} s^{-1}, and with $w \geq 1$ m s^{-1} (black contours). At 2.5 km AGL, (a) stretching term, and (b) tilting term. At 7.5 km AGL, (c) stretching term, and (d) tilting term. Color scale in (a) also applies to (b)-(d).
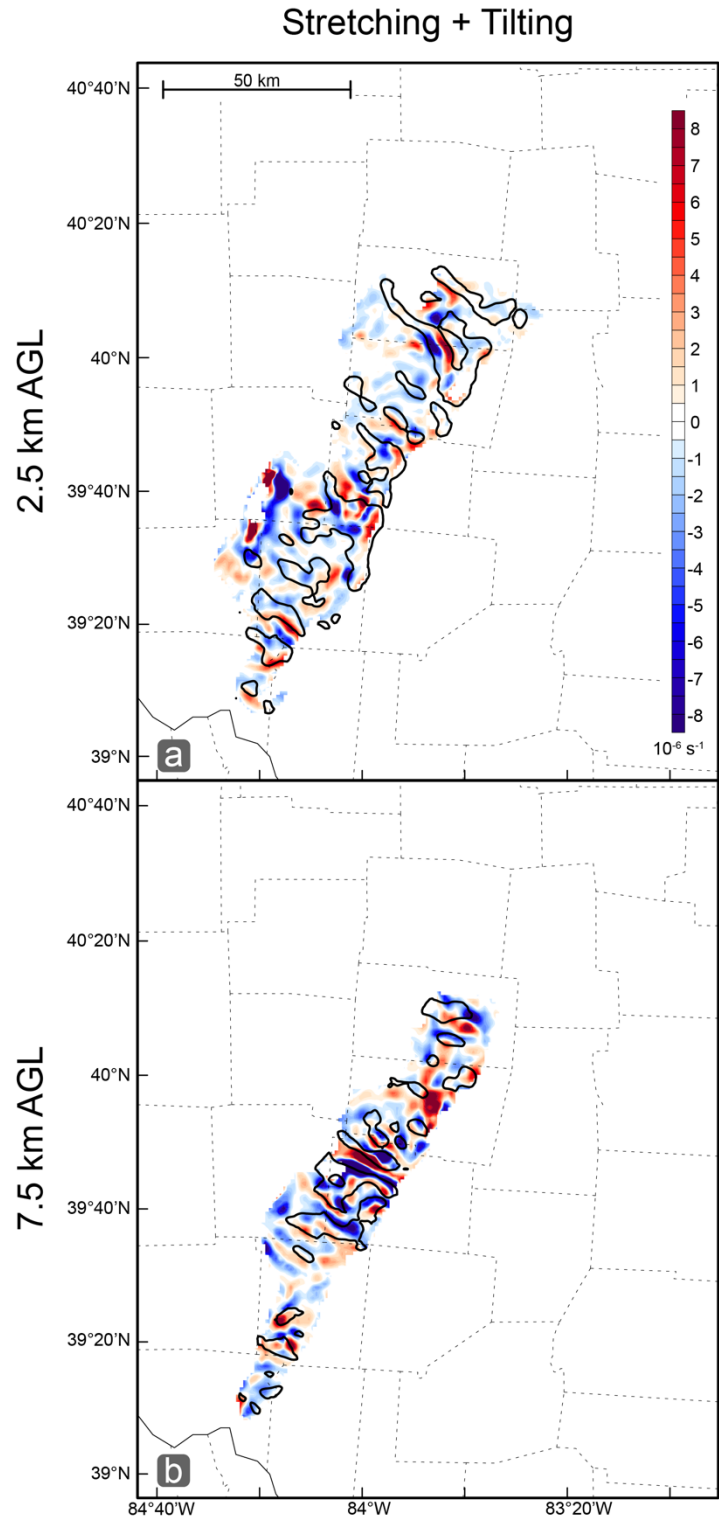
Fig. 14. Total vertical vorticity tendency at (a) 2.5 km AGL, and (b) 7.5 km AGL, from the quad-Doppler analysis valid at 1733 8 June 2003, as given by the total of the tilting and stretching terms provided in Fig. 13. Black contours indicate areas of $w \geq 1$ m s^{-1}. Color scale in (a) also applies to (b).
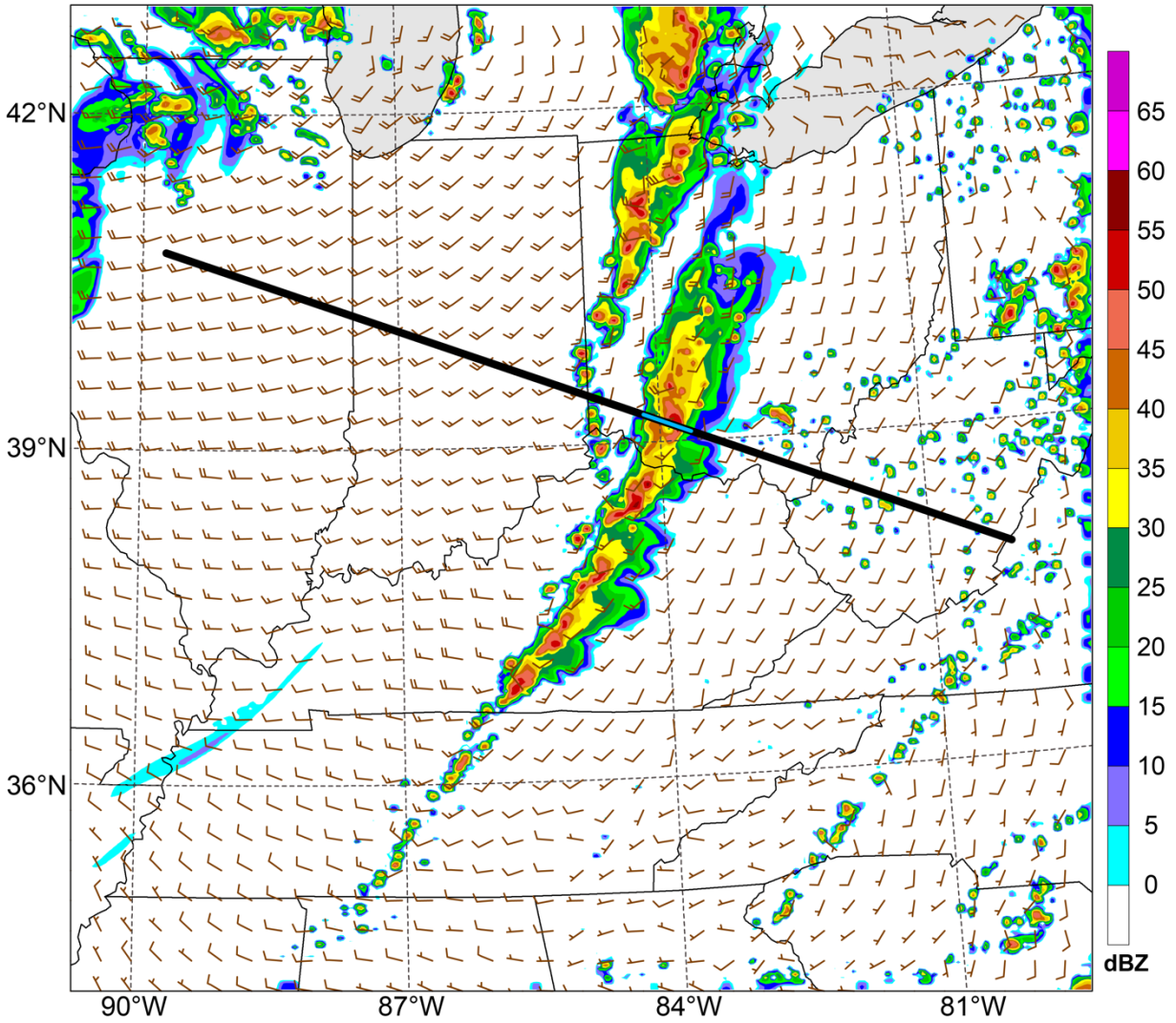
Fig. 15. WRF modeled maximum column reflectivity (dBZ), winds (full barb = 5 m s^{-1}), and the location of the 900 km cross-section (black line; used in Fig. 16), and the location of 50 km cross-sections (light blue line; used in Figs. 17b and 18), all valid at 1730 8 June 2003.
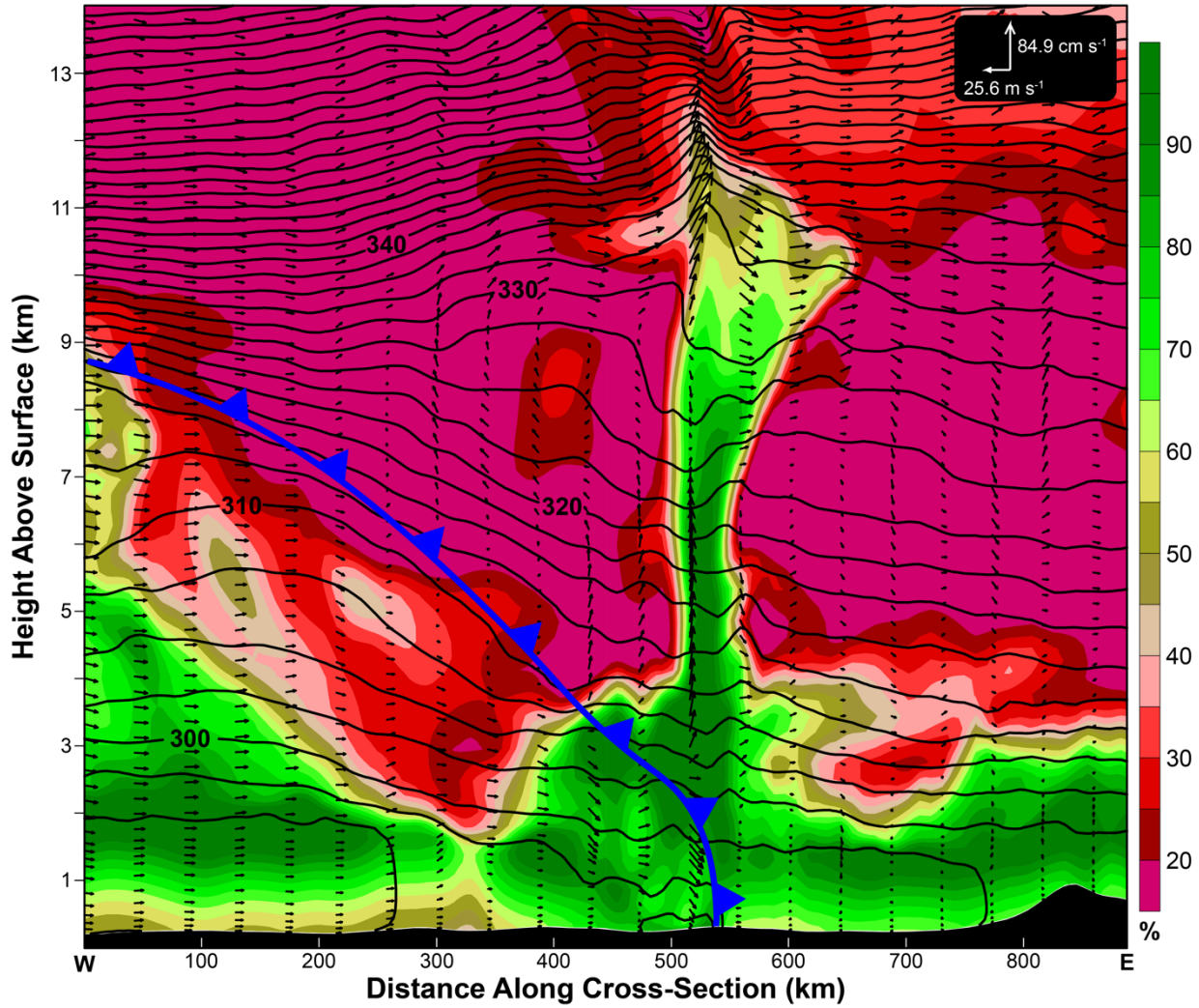
Fig. 16. Cross-section from WRF simulation of relative humidity (filled; %, with respect to water), potential temperature (black contours; every 2.5 K), wind vectors in the plane of the cross-section (m s^{-1}), and subjectively analyzed location of the cold front, all valid at 1730 8 June 2003.
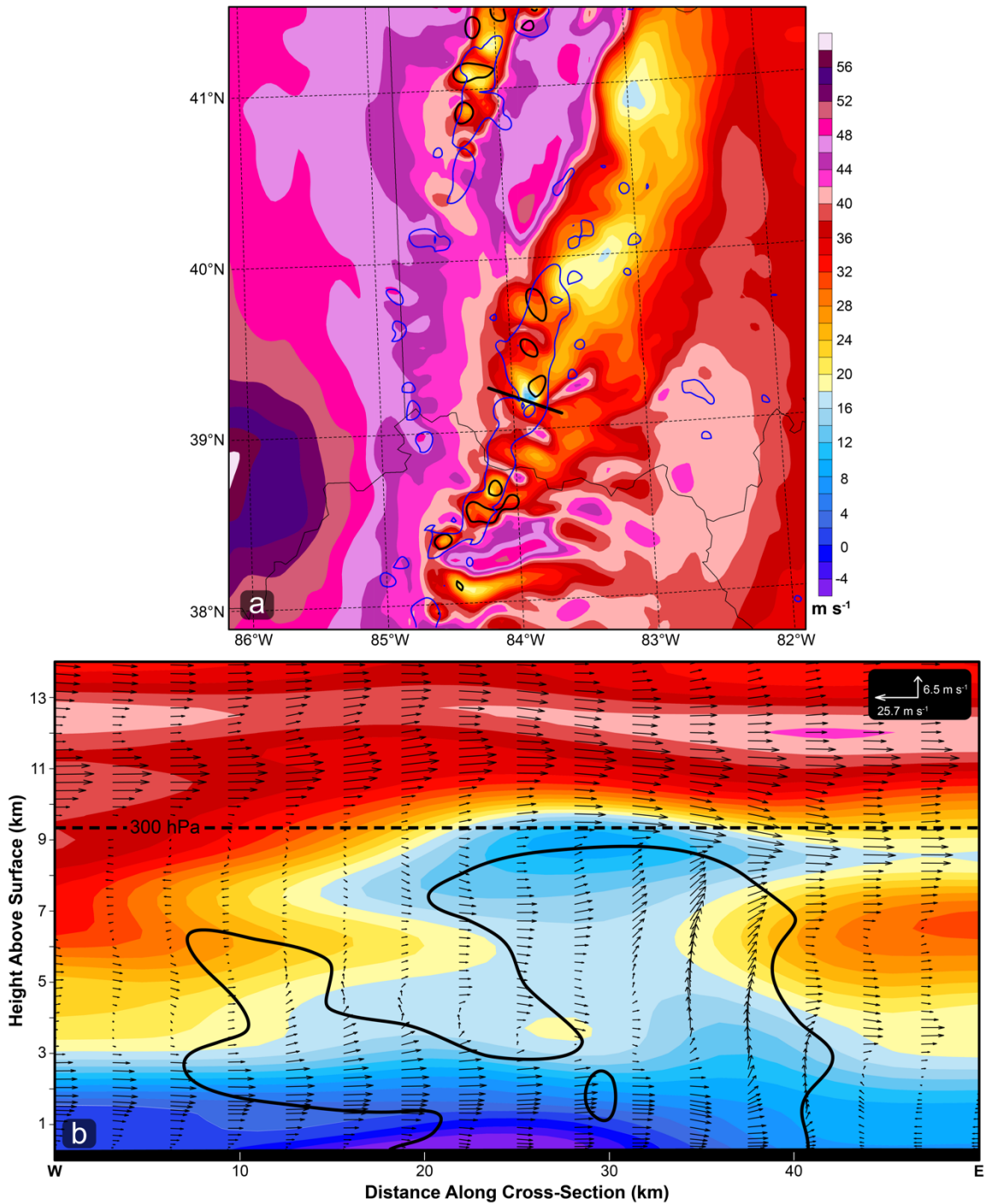
Fig. 17. WRF model analysis valid at 1730 8 June 2003, of (a) wind speed (filled; m s⁻¹) and regions of $w \geq 1$ m s⁻¹ (black contours) at 300 hPa, location of cross-section in (b) (straight black line), and location of reflectivity at 1 km MSL ≥ 30 dBZ (blue contours), and (b) cross-section of winds normal to the cross-section (filled; m s⁻¹; positive is into the page), location of reflectivity ≥ 30 dBZ (black contours), wind vectors (m s⁻¹) rotated to the plane of the cross-section, and the location of the 300 hPa constant pressure surface (dashed black line).
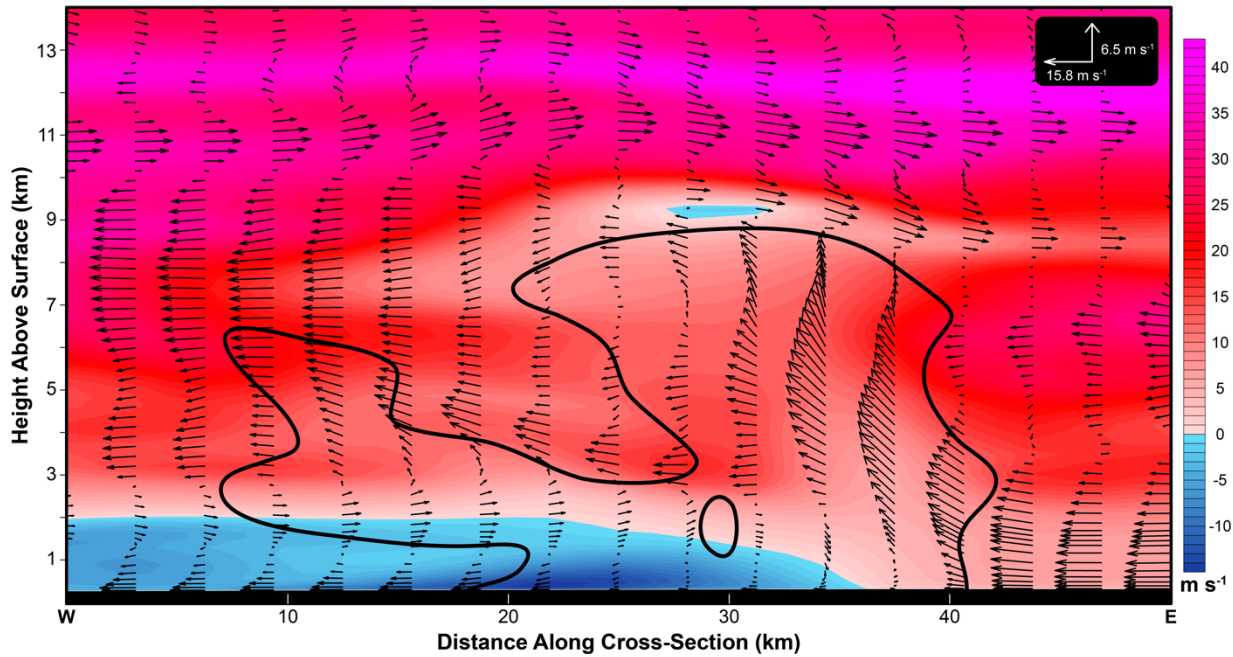
Fig. 18. WRF model analysis valid at 1730 8 June 2003, of storm-relative absolute momentum (filled; m s^{-1}; as defined in Equation 4), location of reflectivity ≥ 30 dBZ (black contours), and storm-relative wind vectors (m s^{-1}) rotated to the plane of the cross-section.
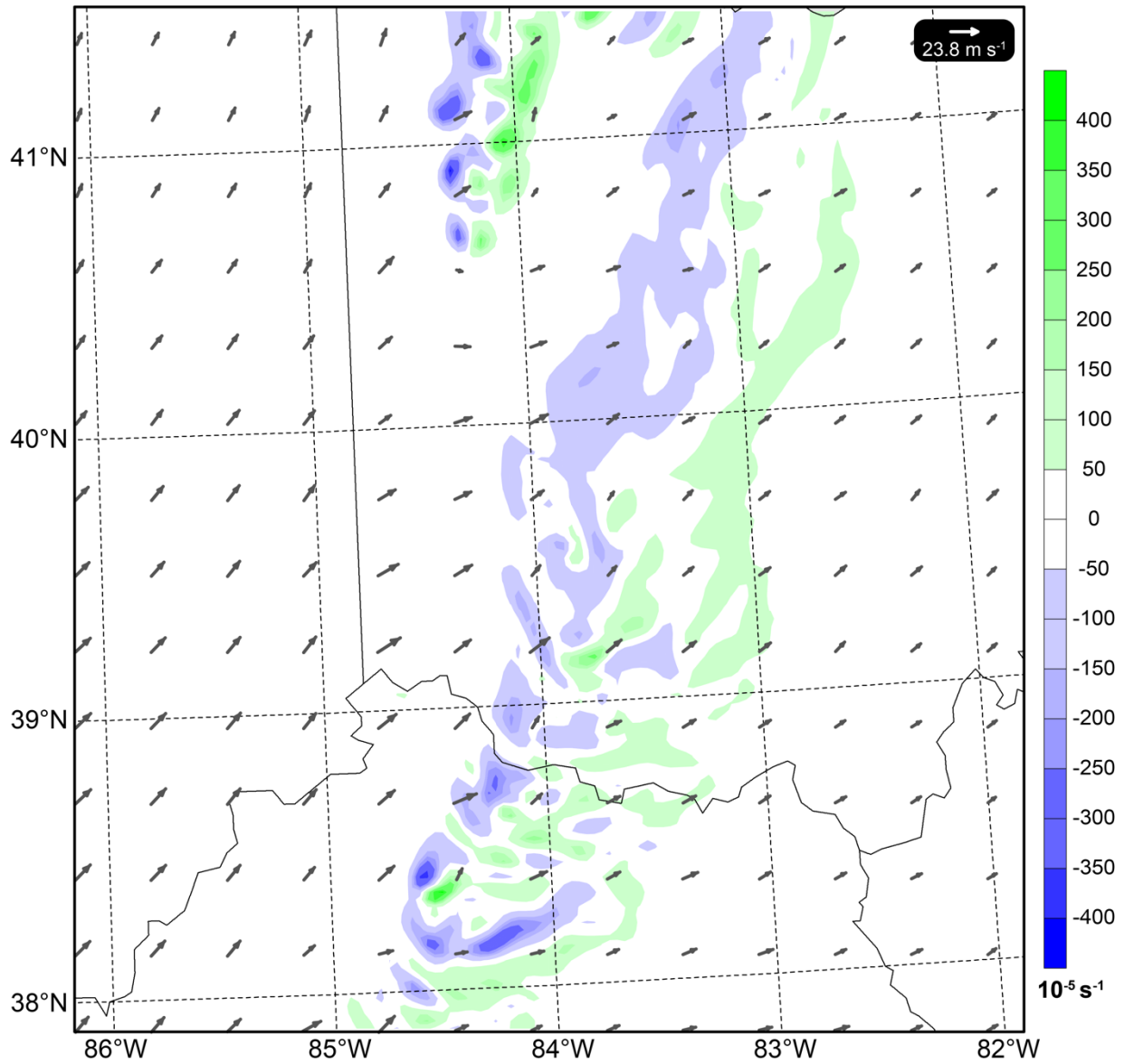
Fig. 19. Relative vertical vorticity (10^{-5} s^{-1}) at 9 km MSL from the WRF model analysis, valid at 1730 8 June 2003, with 0-6 km wind shear vectors (m s^{-1}) overlaid.
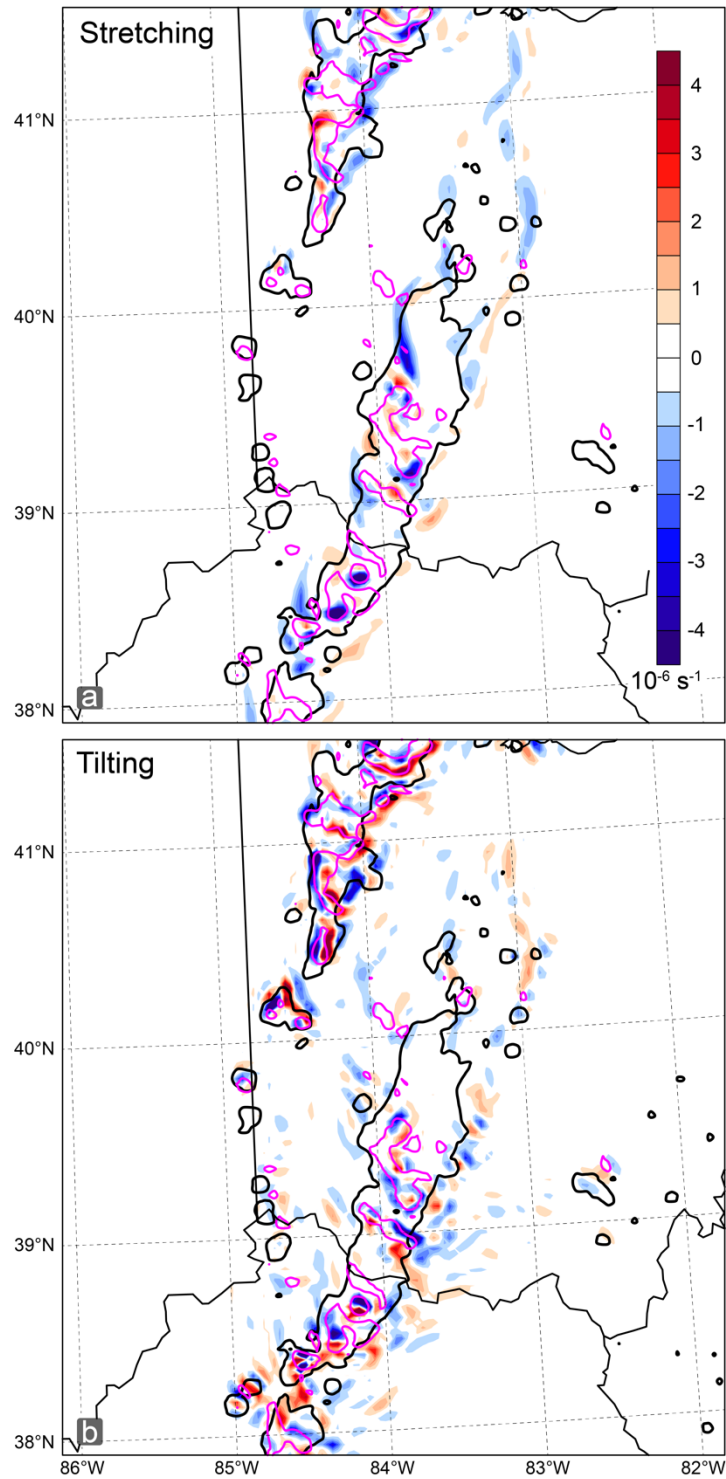
Fig. 20. WRF model analysis valid at 1730 8 June 2003, of the (a) stretching term, and (b) tilting term of the scaled vertical vorticity tendency equation (3) at 7.5 km MSL, each with units of 10^{-6} s^{-1}, regions of $w \geq 1$ m s^{-1} (magenta contours), and the location of maximum column reflectivity ≥ 30 dBZ (black contours). Color scale in (a) also applies to (b).
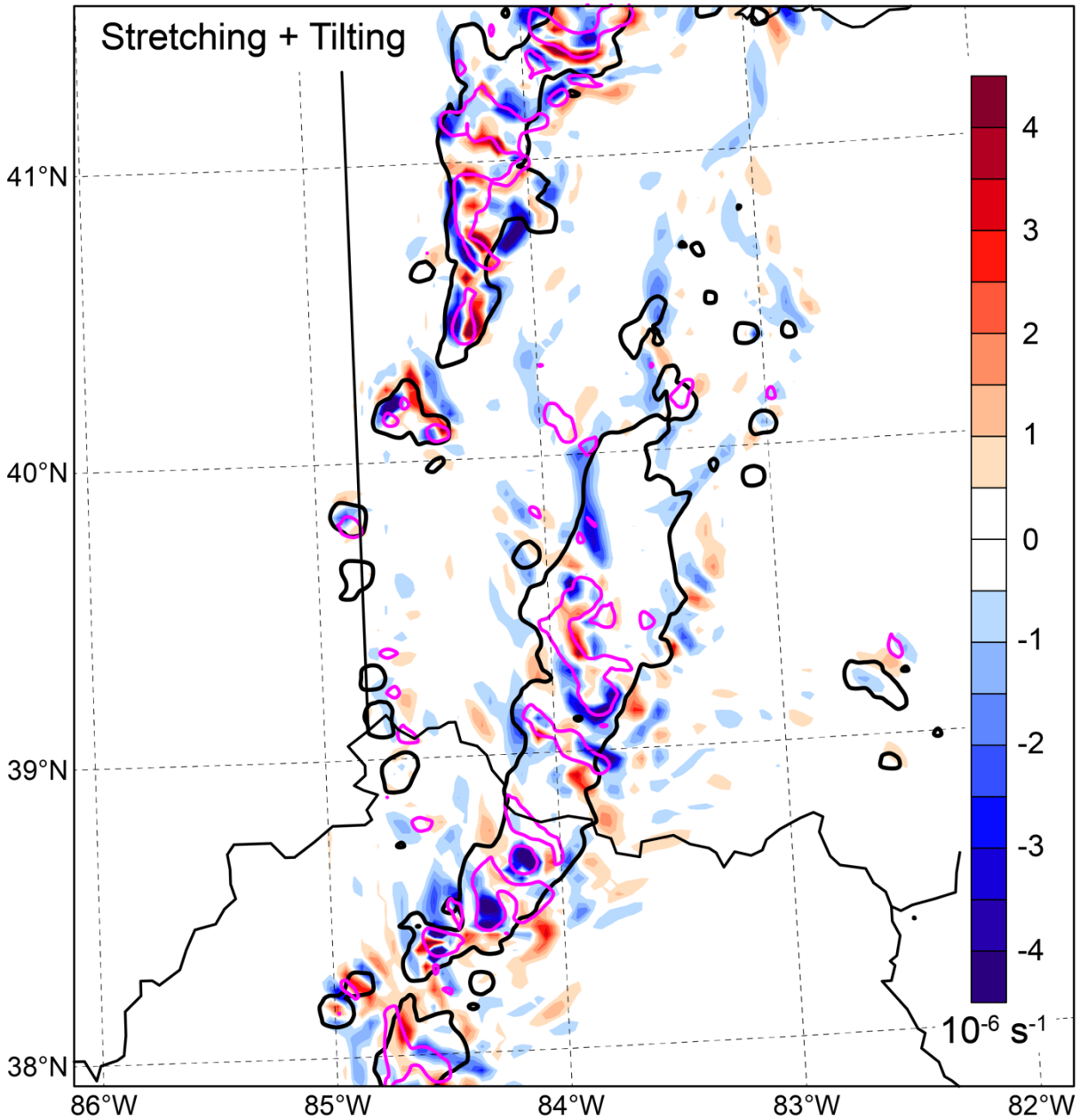
Fig. 21. WRF model analysis valid at 1730 8 June 2003 of the total vertical vorticity tendency at 7.5 km MSL, as given by the sum of the stretching and tilting terms provided in Fig. 20. Magenta contours indicate regions of $w \geq 1$ m s^{-1}, and black contours indicate the location of maximum column reflectivity ≥ 30 dBZ.

Fig. 22. WRF model analysis valid at 1730 8 June 2003 of pressure perturbation (filled; hPa) and $w \geq 2$ m s^{-1} (magenta contours) at 7.5 km MSL. Black contours indicate location of maximum column reflectivity ≥ 30 dBZ. 0-7.5 km wind shear indicated by wind barbs (half barb is 5 m s^{-1}).

References

Atkins, N. T., and M. St. Laurent, 2009a: Bow Echo Mesovortices. Part I: Processes That Influence Their Damaging Potential. *Mon. Wea. Rev.*, **137**, 1497–1513, doi:10.1175/2008MWR2649.1.
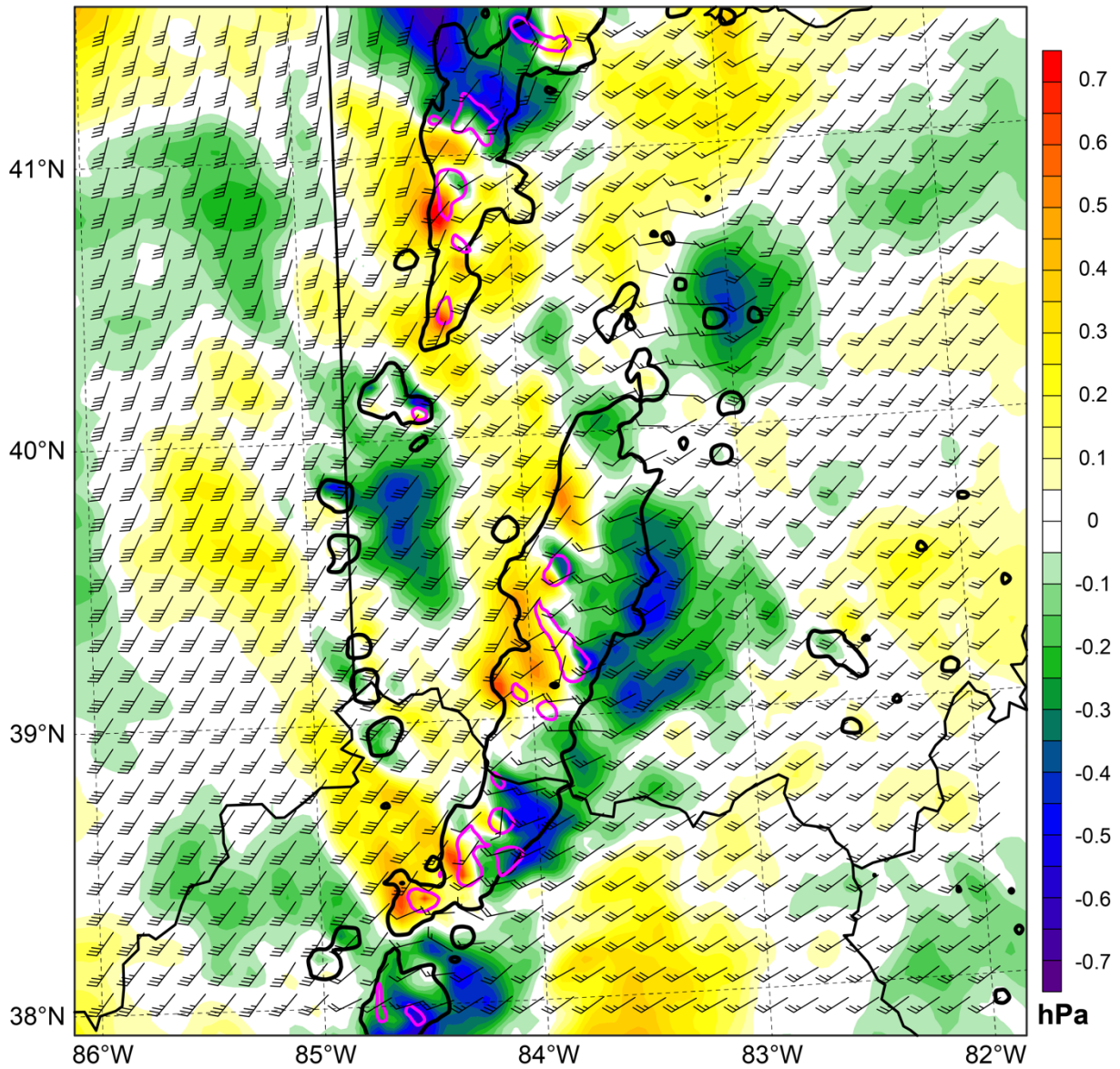
——, and ——, 2009b: Bow Echo Mesovortices. Part II: Their Genesis. *Mon. Wea. Rev.*, **137**, 1514–1532, doi:10.1175/2008MWR2650.1.

——, C. S. Bouchard, R. W. Przybylinski, R. J. Trapp, and G. Schmocker, 2005: Damaging Surface Wind Mechanisms within the 10 June 2003 Saint Louis Bow Echo during BAMEX. *Mon. Wea. Rev.*, **133**, 2275–2296, doi:10.1175/MWR2973.1.

Bell, M. M., W.-C. Lee, C. A. Wolff, and H. Cai, 2013: A Solo-Based Automated Quality Control Algorithm for Airborne Tail Doppler Radar Data. *J. Appl. Meteor. Climatol.*, **52**, 2509–2528, doi:10.1175/JAMC-D-12-0283.1.

Biggerstaff, M. I., and R. A. Houze, 1991a: Kinematic and Precipitation Structure of the 10–11 June 1985 Squall Line. *Mon. Wea. Rev.*, **119**, 3034–3065, doi:10.1175/1520-0493(1991)119<3034:KAPSOT>2.0.CO;2.

——, and ——, 1991b: Midlevel Vorticity Structure of the 10–11 June 1985 Squall Line. *Mon. Wea. Rev.*, **119**, 3066–3079, doi:10.1175/1520-0493(1991)119<3066:MVSOTJ>2.0.CO;2.

Bluestein, H. B., and M. H. Jain, 1985: Formation of Mesoscale Lines of Pirecipitation: Severe Squall Lines in Oklahoma during the Spring. *J. Atmos. Sci.*, **42**, 1711–1732, doi:10.1175/1520-0469(1985)042<1711:FOMLOP>2.0.CO;2.

Cai, H., 2005: Comparison between Tornadic and Nontornadic Mesocyclones Using the Vorticity (Pseudovorticity) Line Technique. *Mon. Wea. Rev.*, **133**, 2535–2551, doi:10.1175/MWR2990.1.

Conzemius, R. J., and M. T. Montgomery, 2010: Mesoscale Convective Vortices in Multiscale, Idealized Simulations: Dependence on Background State, Interdependency with Moist Baroclinic Cyclones, and Comparison with BAMEX Observations. *Mon. Wea. Rev.*, **138**, 1119–1139, doi:10.1175/2009MWR2981.1.

——, R. W. Moore, M. T. Montgomery, and C. A. Davis, 2007: Mesoscale Convective Vortex Formation in a Weakly Sheared Moist Neutral Environment. *J. Atmos. Sci.*, **64**, 1443–1466, doi:10.1175/JAS3898.1.

Correia, J., and R. W. Arritt, 2008: Thermodynamic Properties of Mesoscale Convective Systems Observed during BAMEX. *Mon. Wea. Rev.*, **136**, 4242–4271, doi:10.1175/2008MWR2284.1.

Davis, C. A., and S. B. Trier, 2007: Mesoscale Convective Vortices Observed during BAMEX. Part I: Kinematic and Thermodynamic Structure. *Mon. Wea. Rev.*, **135**, 2029–2049, doi:10.1175/MWR3398.1.

——, and T. J. Galarneau, 2009: The Vertical Structure of Mesoscale Convective Vortices. *J. Atmos. Sci.*, **66**, 686–704, doi:10.1175/2008JAS2819.1.

——, and Coauthors, 2004: The Bow Echo and MCV Experiment: Observations and Opportunities. *Bull. Amer. Meteor. Soc.*, **85**, 1075–1093, doi:10.1175/BAMS-85-8-1075.

Eagleman, J. R., and W. C. Lin, 1977: Severe Thunderstorm Internal Structure from Dual-Doppler Radar Measurements. *J. Appl. Meteor.*, **16**, 1036–1048, doi:10.1175/1520-0450-16.10.1036.

Fankhauser, J. C., 1971: Thunderstorm-Environment Interactions Determined from Aircraft and Radar Observations. *Mon. Wea. Rev.*, **99**, 171–192, doi:10.1175/1520-0493(1971)099<0171:TIDFAA>2.3.CO;2.

Fujita, T., and H. Grandoso, 1968: Split of a Thunderstorm into Anticyclonic and Cyclonic Storms and Their Motion as Determined from Numerical Model Experiments. *J. Atmos. Sci.*, **25**, 416–439, doi:10.1175/1520-0469(1968)025<0416:SOATIA>2.0.CO;2.

Galarneau, T. J., L. F. Bosart, C. A. Davis, and R. McTaggart-Cowan, 2009: Baroclinic Transition of a Long-Lived Mesoscale Convective Vortex. *Mon. Wea. Rev.*, **137**, 562–584, doi:10.1175/2008MWR2651.1.

Gallus, W. A., and R. H. Johnson, 1992: The Momentum Budget of an Intense Midlatitude Squall Line. *J. Atmos. Sci.*, **49**, 422–450, doi:10.1175/1520-0469(1992)049<0422:TMBOAI>2.0.CO;2.

Gao, K., D.-L. Zhang, M. W. Moncrieff, and H.-R. Cho, 1990: Mesoscale Momentum Budget in a Midlatitude Squall Line: A Numerical Case Study. *Mon. Wea. Rev.*, **118**, 1011–1028, doi:10.1175/1520-0493(1990)118<1011:MMBIAM>2.0.CO;2.

Grim, J. A., R. M. Rauber, G. M. McFarquhar, B. F. Jewett, and D. P. Jorgensen, 2009: Development and Forcing of the Rear Inflow Jet in a Rapidly Developing and Decaying Squall Line during BAMEX. *Mon. Wea. Rev.*, **137**, 1206–1229, doi:10.1175/2008MWR2503.1.

Hawblitzel, D. P., F. Zhang, Z. Meng, and C. A. Davis, 2007: Probabilistic Evaluation of the Dynamics and Predictability of the Mesoscale Convective Vortex of 10–13 June 2003. *Mon. Wea. Rev.*, **135**, 1544–1563, doi:10.1175/MWR3346.1.

Hildebrand, P. H., and Coauthors, 1996: The ELDORA/ASTRAIA airborne Doppler weather radar: High-resolution observations from TOGA COARE. *Bull. Amer. Meteor. Soc.*, **77**, 213–232, doi:10.1175/1520-0477(1996)077<0213:TEADWR>2.0.CO;2.

Hong, S.-Y., Y. Noh, and J. Dudhia, 2006: A New Vertical Diffusion Package with an Explicit Treatment of Entrainment Processes. *Mon. Wea. Rev.*, **134**, 2318–2341, doi:10.1175/MWR3199.1.

Houze, R. A., 1973: A climatological study of vertical transports by cumulus-scale convection. *J. Atmos. Sci.*, **30**, 1112–1123, doi:10.1175/1520-0469(1973)030<1112:ACSOVT>2.0.CO;2.

——, 2004: Mesoscale convective systems. *Rev. Geophys.*, **42**, RG4003, doi:10.1029/2004RG000150.

——, S. S. Chen, D. E. Kingsmill, Y. Serra, and S. E. Yuter, 2000: Convection over the Pacific Warm Pool in relation to the Atmospheric Kelvin-Rossby Wave. *J. Atmos. Sci.*, **57**, 3058–3089, doi:10.1175/1520-0469(2000)057<3058:COTPWP>2.0.CO;2.

Iacono, M. J., J. S. Delamere, E. J. Mlawer, M. W. Shephard, S. a. Clough, and W. D. Collins, 2008: Radiative forcing by long-lived greenhouse gases: Calculations with the AER radiative transfer models. *J. Geophys. Res. Atmos.*, **113**, 2–9, doi:10.1029/2008JD009944.

James, E. P., and R. H. Johnson, 2010: Patterns of Precipitation and Mesolow Evolution in Midlatitude Mesoscale Convective Vortices. *Mon. Wea. Rev.*, **138**, 909–931, doi:10.1175/2009MWR3076.1.

Janjić, Z. I., 1994: The Step-Mountain Eta Coordinate Model: Further Developments of the Convection, Viscous Sublayer, and Turbulence Closure Schemes. *Mon. Wea. Rev.*, **122**, 927–945, doi:10.1175/1520-0493(1994)122<0927:TSMECM>2.0.CO;2.

Jirak, I. L., and W. R. Cotton, 2007: Observational Analysis of the Predictability of Mesoscale Convective Systems. *Wea. Forecasting*, **22**, 813–838, doi:10.1175/WAF1012.1.

Jorgensen, D. P., T. Matejka, and J. D. DuGranrut, 1996: Multi-beam techniques for deriving wind fields from airborne doppler radars. *Meteor. Atmos. Phys.*, **59**, 83–104, doi:10.1007/BF01032002.

Kain, J. S., 2004: The Kain–Fritsch Convective Parameterization: An Update. *J. Appl. Meteor.*, **43**, 170–181, doi:10.1175/1520-0450(2004)043<0170:TKCPAU>2.0.CO;2.

Kropfli, R. A., and L. S. Miller, 1976: Kinematic Structure and Flux Quantities in a Convective Storm from Dual-Doppler Radar Observations. *J. Atmos. Sci.*, **33**, 520–529, doi:10.1175/1520-0469(1976)033<0520:KSAFQI>2.0.CO;2.

Leise, J. A., 1982: *A multidimensional scale-telescoped filter and data extension package*. NOAA tech. U.S. Dept. of Commerce, National Oceanic and Atmospheric Administration, Environmental Research Laboraties, Boulder, CO, 19 pp.

LeMone, M. A., 1983: Momentum Transport by a Line of Cumulonimbus. *J. Atmos. Sci.*, **40**, 1815–1834, doi:10.1175/1520-0469(1983)040<1815:MTBALO>2.0.CO;2.

——, and M. W. Moncrieff, 1994: Momentum and Mass Transport by Convective Bands: Comparisons of Highly Idealized Dynamical Models to Observations. *J. Atmos. Sci.*, **51**, 281–305, doi:10.1175/1520-0469(1994)051<0281:MAMTBC>2.0.CO;2.

Lipps, F. B., and R. S. Hemler, 1991: Numerical Modeling of a Midlatitude Squall Line: Features of the Convection and Vertical Momentum Flux. *J. Atmos. Sci.*, **48**, 1909–1929, doi:10.1175/1520-0469(1991)048<1909:NMOAMS>2.0.CO;2.

Mahoney, K. M., G. M. Lackmann, and M. D. Parker, 2009: The Role of Momentum Transport in the Motion of a Quasi-Idealized Mesoscale Convective System. *Mon. Wea. Rev.*, **137**, 3316–3338, doi:10.1175/2009MWR2895.1.

Mechem, D. B., S. S. Chen, and R. A. Houze, 2006: Momentum transport processes in the stratiform regions of mesoscale convective systems over the western Pacific warm pool. *Quart. J. Roy. Meteor. Soc.*, **132**, 709–736, doi:10.1256/qj.04.141.

Meng, Z., and F. Zhang, 2007: Tests of an Ensemble Kalman Filter for Mesoscale and Regional-Scale Data Assimilation. Part II: Imperfect Model Experiments. *Mon. Wea. Rev.*, **135**, 1403–1423, doi:10.1175/MWR3352.1.

——, and ——, 2008: Tests of an Ensemble Kalman Filter for Mesoscale and Regional-Scale Data Assimilation. Part III: Comparison with 3DVAR in a Real-Data Case Study. *Mon. Wea. Rev.*, **136**, 522–540, doi:10.1175/2007MWR2106.1.

Morrison, H., G. Thompson, and V. Tatarskii, 2009: Impact of Cloud Microphysics on the Development of Trailing Stratiform Precipitation in a Simulated Squall Line: Comparison of One- and Two-Moment Schemes. *Mon. Wea. Rev.*, **137**, 991–1007, doi:10.1175/2008MWR2556.1.

National Centers for Environmental Prediction NOAA, U.S. Department of Commerce, N. W. S., 2005: NCEP North American Regional Reanalysis (NARR). http://rda.ucar.edu/datasets/ds608.0/ (Accessed January 27, 2015).

Newton, C. W., 1950: Structure and Mechanism of the Prefrontal Squall Line. *J. Meteor.*, **7**, 210–222, doi:10.1175/1520-0469(1950)007<0210:SAMOTP>2.0.CO;2.

——, and H. R. Newton, 1959: Dynamical Interactions Between Large Convective Clouds and Environment with Vertical Shear. *J. Meteor.*, **16**, 483–496, doi:10.1175/1520-0469(1959)016<0483:DIBLCC>2.0.CO;2.

Oye, R., C. Mueller, and S. Smith, 1995: Software for radar translation, visualization, editing, and interpolation. *Preprints, 27th Conf. on Radar Meteorology*, Vail, CO, Amer. Meteor. Soc., 359–361.

Ross, B. B., and I. Orlanski, 1978: The Circulation Associated with a Cold Front. Part II: Moist Case. *J. Atmos. Sci.*, **35**, 445–465, doi:10.1175/1520-0469(1978)035<0445:TCAWAC>2.0.CO;2.

Rotunno, R., and J. B. Klemp, 1982: The Influence of the Shear-Induced Pressure Gradient on Thunderstorm Motion. *Mon. Wea. Rev.*, **110**, 136–151, doi:10.1175/1520-0493(1982)110<0136:TIOTSI>2.0.CO;2.

——, ——, and M. L. Weisman, 1988: A Theory for Strong, Long-Lived Squall Lines. *J. Atmos. Sci.*, **45**, 463–485, doi:10.1175/1520-0469(1988)045<0463:ATFSLL>2.0.CO;2.

Sanders, F., and K. A. Emanuel, 1977: The Momentum Budget and Temporal Evolution of a Mesoscale Convective System. *J. Atmos. Sci.*, **34**, 322–330, doi:10.1175/1520-0469(1977)034<0322:TMBATE>2.0.CO;2.

Schlesinger, R. E., 1975: A Three-Dimensional Numerical Model of an Isolated Deep Convective Cloud: Preliminary Results. *J. Atmos. Sci.*, **32**, 934–957, doi:10.1175/1520-0469(1975)032<0934:ATDNMO>2.0.CO;2.

Skamarock, W. C., and Coauthors, 2008: A Description of the Advanced Research WRF Version 3. *NCAR Tech. Note*, **TN-475+STR**, 113.

Smith, A. M., G. M. McFarquhar, R. M. Rauber, J. A. Grim, M. S. Timlin, B. F. Jewett, and D. P. Jorgensen, 2009: Microphysical and Thermodynamic Structure and Evolution of the Trailing Stratiform Regions of Mesoscale Convective Systems during BAMEX. Part I: Observations. *Mon. Wea. Rev.*, **137**, 1165–1185, doi:10.1175/2008MWR2504.1.

Stoelinga, M. T., J. D. Locatelli, R. D. Schwartz, and P. V. Hobbs, 2003: Is a Cold Pool Necessary for the Maintenance of a Squall Line Produced by a Cold Front Aloft? *Mon. Wea. Rev.*, **131**, 95–115, doi:10.1175/1520-0493(2003)131<0095:IACPNF>2.0.CO;2.

Storm, B. A., M. D. Parker, and D. P. Jorgensen, 2007: A Convective Line with Leading Stratiform Precipitation from BAMEX. *Mon. Wea. Rev.*, **135**, 1769–1785, doi:10.1175/MWR3392.1.

Thompson, G., P. R. Field, R. M. Rasmussen, and W. D. Hall, 2008: Explicit Forecasts of Winter Precipitation Using an Improved Bulk Microphysics Scheme. Part II: Implementation of a New Snow Parameterization. *Mon. Wea. Rev.*, **136**, 5095–5115, doi:10.1175/2008MWR2387.1.

Trier, S. B., and C. A. Davis, 2007: Mesoscale Convective Vortices Observed during BAMEX. Part II: Influences on Secondary Deep Convection. *Mon. Wea. Rev.*, **135**, 2051–2075, doi:10.1175/MWR3399.1.

——, M. A. LeMone, and W. C. Skamarock, 1998: Effect of Three-Dimensional Structure on the Stormwide Horizontal Accelerations and Momentum Budget of a Simulated Squall Line. *Mon. Wea. Rev.*, **126**, 2580–2598, doi:10.1175/1520-0493(1998)126<2580:EOTDSO>2.0.CO;2.

Wakimoto, R. M., H. Cai, and H. V. Murphey, 2004: The Superior, Nebraska, Supercell During BAMEX. *Bull. Amer. Meteor. Soc.*, **85**, 1095–1106, doi:10.1175/BAMS-85-8-1095.

——, H. V. Murphey, C. A. Davis, and N. T. Atkins, 2006a: High Winds Generated by Bow Echoes. Part II: The Relationship between the Mesovortices and Damaging Straight-Line Winds. *Mon. Wea. Rev.*, **134**, 2813–2829, doi:10.1175/MWR3216.1.

——, ——, A. Nester, D. P. Jorgensen, and N. T. Atkins, 2006b: High Winds Generated by Bow Echoes. Part I: Overview of the Omaha Bow Echo 5 July 2003 Storm during BAMEX. *Mon. Wea. Rev.*, **134**, 2793–2812, doi:10.1175/MWR3215.1.

——, P. Stauffer, and W.-C. Lee, 2015: The Vertical Vorticity Structure within a Squall Line Observed during BAMEX: Banded Vorticity Features and the Evolution of a Bowing Segment. *Mon. Wea. Rev.*, **143**, 341–362, doi:10.1175/MWR-D-14-00246.1.

Wang, P. K., S.-H. Su, M. Setvak, H. Lin, and R. M. Rabin, 2010: Ship wave signature at the cloud top of deep convective storms. *Atmos. Res.*, **97**, 294–302, doi:10.1016/j.atmosres.2010.03.015.

Wheatley, D. M., and R. J. Trapp, 2008: The Effect of Mesoscale Heterogeneity on the Genesis and Structure of Mesovortices within Quasi-Linear Convective Systems. *Mon. Wea. Rev.*, **136**, 4220–4241, doi:10.1175/2008MWR2294.1.

——, ——, and N. T. Atkins, 2006: Radar and Damage Analysis of Severe Bow Echoes Observed during BAMEX. *Mon. Wea. Rev.*, **134**, 791–806, doi:10.1175/MWR3100.1.

Wilhelmson, R. B., 1974: The Life Cycle of a Thunderstorm in Three Dimensions. *J. Atmos. Sci.*, **31**, 1629–1651, doi:10.1175/1520-0469(1974)031<1629:TLCOAT>2.0.CO;2.

——, and J. B. Klemp, 1978: A Numerical Study of Storm Splitting that Leads to Long-Lived Storms. *J. Atmos. Sci.*, **35**, 1974–1986, doi:10.1175/1520-0469(1978)035<1974:ANSOSS>2.0.CO;2.

Wyss, J., and K. A. Emanuel, 1988: The Pre-storm Environment of Midlatitude Prefrontal Squall Lines. *Mon. Wea. Rev.*, **116**, 790–794, doi:10.1175/1520-0493(1988)116<0790:TPSEOM>2.0.CO;2.

Yang, M.-J., and R. A. Houze, 1996: Momentum Budget of a Squall Line with Trailing Stratiform Precipitation: Calculations with a High-Resolution Numerical Model. *J. Atmos. Sci.*, **53**, 3629–3652, doi:10.1175/1520-0469(1996)053<3629:MBOASL>2.0.CO;2.

Zhang, D.-L., K. Gao, and D. B. Parsons, 1989: Numerical Simulation of an Intense Squall Line during 10–11 June 1985 PRE-STORM. Part I: Model Verification. *Mon. Wea. Rev.*, **117**, 960–994, doi:10.1175/1520-0493(1989)117<0960:NSOAIS>2.0.CO;2.